J. Mech. Phys. Solids 192 (2024) 105828



Contents lists available at ScienceDirect

Journal of the Mechanics and Physics of Solids

journal homepage: www.elsevier.com/locate/jmps





Effects of adhesive and frictional contacts on the nanoindentation of two-dimensional material drumheads

Yifan Rao [a], Nanshu Lu [a,b,*]

[a] Center for Mechanics of Solids, Structures and Materials, Department of Aerospace Engineering and Engineering Mechanics, The University of Texas at Austin, Austin, TX, 78712, United States
[b] Walker Department of Mechanical Engineering, The University of Texas at Austin, Austin, TX, 78712, United States

ARTICLE INFO

Keywords:
Indentation
Membrane
Adhesion
Sliding
Interface

ABSTRACT

Nanoindentation of suspended circular thin films, dubbed drumhead nanoindentation, is a widely adopted technique for characterizing the mechanical properties of micro- or nano-membranes, including atomically thin two-dimensional (2D) materials. This method involves suspending an ultrathin specimen over a circular microhole and applying a precise indenting force at the center using an atomic force microscope (AFM) probe. Classical solutions assuming a point load and a fixed edge, which are referred to as Schwerin-type solutions, are commonly used to estimate Young's modulus of the membrane material out of load–deflection measurements. However, given the widespread experimental evidence for adhesive and frictional contacts between the probe tip and the membrane, as well as sliding between the membrane and its supporting substrate, quantitative investigations of the effects of these interactions are required. In this paper, we formulate a boundary value problem to rigorously model such effects, ensuring relevance to experimental operations. Our numerical analyses reveal that the adhesive effect at the tip-membrane interface diminishes as the indentation depth increases or the tip size decreases. Furthermore, frictional interactions at this interface shift the maximum membrane stress from the center to the tip-membrane contact line with increasing indentation depth and interfacial shear stress. At large indentation depths, the size of the indenter tip and the sliding of the membrane-substrate are found to have a large effect on the indentation load–deflection relationship. Thus, we propose a new approximate formula for this relationship assuming a non-adhesive and frictionless spherical tip of a finite radius and a slippery contact with the supporting substrate. This formula is more accurate than the widely used Schwerin-type solution. It can be used to simultaneously extract the in-plane stiffness of the membrane and the shear strength at the membrane-substrate interface.

1. Introduction

Drumhead nanoindentation testing, where an ultrathin membrane is suspended over a circular microhole and indented in the center by a sharp probe such as an atomic force microscope (AFM) tip, is a widely used experimental technique to measure the mechanical properties of micro- and nano-membranes due to its straightforward sample preparation and operation and ease of formulation (Maner et al., 2004; Begley and Mackin, 2004; Akinwande et al., 2017; Ozaki et al., 2018; Tu et al., 2018; Yang et al., 2019). This method is particularly popular for testing two-dimensional (2D) materials such as graphene and MoS_2 with

* Corresponding author.
E-mail address: nanshulu@utexas.edu (N. Lu).

https://doi.org/10.1016/j.jmps.2024.105828
Received 14 June 2024; Received in revised form 7 August 2024; Accepted 14 August 2024
Available online 22 August 2024
0022-5096/© 2024 Elsevier Ltd. All rights are reserved, including those for text and data mining, AI training, and similar technologies.

atomic-level thinness, which presents challenges for conventional testing methods such as uniaxial tensile tests (Liu and Wu, 2016; Al-Quraishi et al., 2020; Di Giorgio et al., 2022). Pioneering studies by Lee et al. (2008) and Bertolazzi et al. (2011) have shown the efficacy of this method in estimating the Young's modulus and the breaking strength of monolayer graphene and MoS_2 through load–deflection measurements. Furthermore, this method has been extended to investigate the mechanical characteristics of multilayer 2D materials (Ruiz-Vargas et al., 2011; Castellanos-Gomez et al., 2012a,b; Lee et al., 2013; Lin et al., 2014; Falin et al., 2017; Zhang et al., 2020). Separately, drumhead nanoindentation is crucial for the strain engineering of 2D-material-based devices (Cartamil-Bueno et al., 2017; Dai et al., 2019; Shi and Cheng, 2020; Han et al., 2021; Jang et al., 2022; Han et al., 2022). For instance, precise control over the indentation parameters, such as indentation depth, allows the alteration of the band-piezoelectric effect of graphene (Wang et al., 2015) and the band gap of MoS_2 (Manzeli et al., 2015).

The mechanics analysis of indentation on freestanding membranes was first pioneered by Schwerin (1929), who identified a cubic dependence of the indentation force on the indentation depth (i.e., $F \propto d^3$) by assuming a point load and a fixed edge. Schwerin's solution was derived by equating the work done by the probe with the stretching energy stored in the membrane, while neglecting its bending stiffness. Over the years, the increased precision and resolution of indentation technology have expanded its application to characterize ultrathin specimens. Micro- and nano-membranes inherently experience prestresses due to growth or transfer processes (Mougin et al., 2003; Zhou et al., 2013a; Cao et al., 2014), leading to a proposed linear load–deflection relation (i.e., $F \propto d$) at small indentation depths (Wan et al., 2003; Komaragiri et al., 2005). Consequently, a widely used formulation that combines linear and cubic behaviors has been extensively applied to fit the load–deflection data obtained in drumhead nanoindentation tests (Lee et al., 2008; Ruiz-Vargas et al., 2011; Cao and Gao, 2019). However, this Schwerin-type approximation faces challenges in accurately capturing the transition from linear behavior under small deflections to cubic behavior under large deflections (Vella and Davidovitch, 2017). Furthermore, as the thickness of the membrane increases, the effect of bending stiffness becomes significant in the analysis of drumhead nanoindentation (Castellanos-Gomez et al., 2012a; Chandler and Vella, 2020).

The point load assumption in drumhead nanoindentation analysis introduces stress singularities, posing challenges in accurately determining the maximum membrane stress before rupture, defined as the breaking strength. To address this, Bhatia and Nachbar (1968) provided a widely used formulation based on a non-adhesive and frictionless spherical indentation tip to estimate the breaking strength using the fracture force ($F_{\max}$) and the radius of the tip (R). However, at the micro- or nano-scale, adhesive forces such as van der Waals (vdW) interactions between the tip and the membrane are commonly observed, often resulting in a "pull-in" instability where minute interactions can form at the tip-membrane interface when the tip slowly approaches the membrane (Lee et al., 2008; Zhou et al., 2013b,c; Jiang and Zhu, 2015; Rokni and Lu, 2020). Beyond mere adhesion in the normal direction, tangential frictional interactions between the indenter and the membrane have also been reported for 2D materials, especially considering the formation of mechanically activated covalent bonds at the tip-2D material interface (Deng et al., 2013; Dong et al., 2013; Kumar and Parks, 2015; Rokni and Lu, 2020; Zhan et al., 2021; Zhang et al., 2023). Although extensive research has been conducted on the effects of tip size and geometry (Begley and Mackin, 2004; Komaragiri et al., 2005; Vella and Davidovitch, 2017; Chandler and Vella, 2020; Segovia et al., 2021), the quantitative understanding of the effects of tip-membrane interfacial interactions, which include both normal adhesion and tangential shear, remains a subject of ongoing research.

In addition to forming an interface with the indenter, the membrane also has an interface with its supporting substrate beyond its circular edge. Recent experimental and theoretical investigations have reported interfacial slippage of 2D materials against their supporting substrates during indentation or bulging (Kitt et al., 2013; Dai et al., 2018, 2020; Dai and Lu, 2021; Dai et al., 2022; Sun et al., 2022; Rao et al., 2023). This slippage is attributed to the weak shear resistance provided by the vdW interactions at the membrane-substrate interface. In particular, Dai and Lu (2021) demonstrated that this interfacial slippage is evidenced by the fact that the measured cubic stiffness (i.e., F/d^3) of monolayer graphene at large indentation depths is lower than that predicted by the Schwerin-type solution. In the study by Dai and Lu (2021), prestress is neglected, as its influence is considered to diminish at large deflections. Sun et al. (2022) provided an approximate formulation that incorporates prestress, membrane elasticity, and a sliding edge based on the assumption of a point load. However, this approach lacks numerical validation. Thus, the effects of interfacial slippage on drumhead nanoindentation using a spherical tip of finite radius still warrant further investigation.

To elucidate the effects of the aforementioned interfacial interactions in drumhead nanoindentation, we establish a comprehensive theoretical framework incorporating membrane prestress, membrane elasticity, finite tip size, adhesive and frictional tip-membrane interactions, as well as the slippage at the membrane-substrate interface in this paper. It is structured as follows: Section 2 introduces the problem with the corresponding experimental evidence. Section 3 outlines the model formulation, emphasizing the various boundary conditions at the contact lines between the tip and the membrane, as well as between the membrane and the substrate. In Section 4, we detail the numerical implementation of established models. Section 5 presents the numerical results, including comparisons between the established and proposed approximations, and discussions of the effects of various interfacial interactions on the load–deflection relationship and membrane stress distributions. Finally, Section 6 provides concluding remarks.

2. Problem description

In drumhead nanoindentation tests, interfacial interactions are consistently manifest. Various contributing factors, including vdW interactions and covalent bonds, govern the adhesion and friction between the AFM tip and the suspended specimen (Dong et al., 2013; Kumar and Parks, 2015; Rokni and Lu, 2020). The tip is often simplified as a spherical cap with a finite radius R (Lee et al., 2008). Meanwhile, the slippage of the membrane against its supporting substrate is facilitated by the limited fixation at the periphery of the cavity, mainly due to the relatively weak vdW interactions at the interface between the membrane and the substrate (Dai

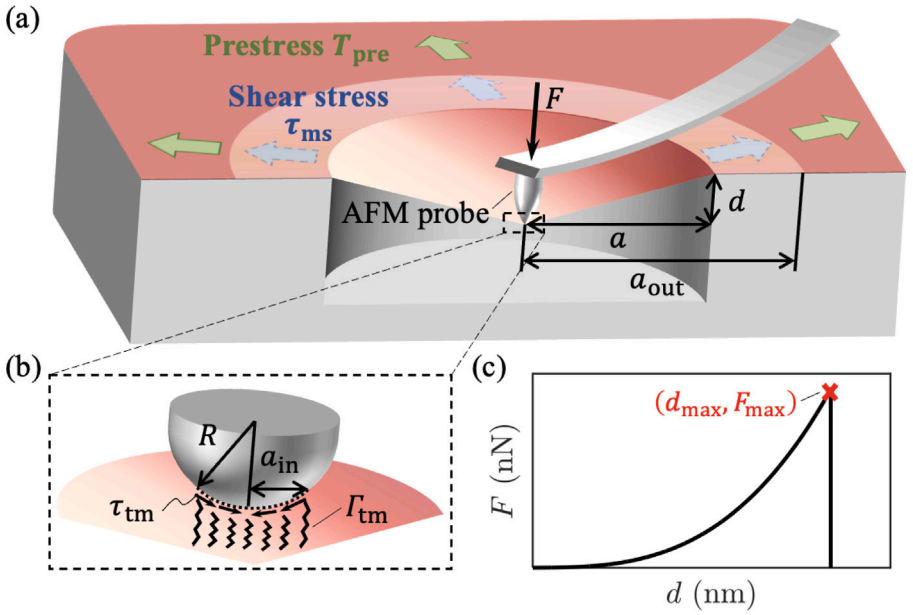


Fig. 1. (a) Schematic illustration and notations for drumhead nanoindentation using an atomic force microscope (AFM) probe with a spherical tip, considering the sliding between the membrane and the supporting substrate, as well as the adhesive and/or frictional contact between the tip and the indented membrane as illustrated in the magnified view in (b). (c) A typical indentation load–deflection curve with the red cross indicating the maximum force (F_{max}) and deflection (d_{max}) right before membrane rupture. This paper assumes constant adhesion energy (Γ_{tm} [J/m^2]) and shear stress (τ_{tm} [N/m^2]) at the tip-membrane interface, as well as constant shear stress (τ_{ms} [N/m^2]) at the membrane-substrate interface. Furthermore, the BVP assumes that the contact radii at the tip-membrane interface (a_{in}) and the membrane-substrate interface (a_{out}) are unknown a priori.

and Lu, 2021; Sun et al., 2022). Figure 1a illustrates the nanoindentation of a membrane suspended on a cylindrical cavity of radius a formed on a rigid substrate, taking into account these prestress, finite tip size, and various interfacial interactions. To assess the amount of energy gained during the tip-membrane attachment, we assume a constant adhesion energy per unit area (Γ_{tm} [J/m^2]) in the contact area between the tip and the membrane (refer to Fig. 1b). To assess shear resistance, we assume constant shear stress (traction) (τ_{tm} [N/m^2]) at the tip-membrane interface, as well as constant shear stress (traction) (τ_{ms} [N/m^2]) at the membrane-substrate interface during drumhead nanoindentation, respectively. Changes in adhesion energy at the membrane-substrate interface can be disregarded, as the edge of the cavity inhibits the normal detachment of the membrane during indentation. Different normal and tangential traction-separation laws, beyond the constant ones adopted here, can be incorporated and discussed in future research (Jiang and Park, 2015; Yuan and Wang, 2021; Rao et al., 2023). It should be noted that, due to adhesive and frictional contacts, the contact radii at the tip-membrane interface (a_{in}) and the membrane-substrate interface (a_{out}) are unknown a priori, causing complexity in the formulation of the boundary value problem (BVP). Additionally, the membrane prestress (T_{pre} [N/m]) is considered uniform and isotropic in this paper. We assume a neglected bending rigidity as this paper focuses on ultrathin materials, particularly monolayer 2D materials like monolayer graphene.

The relationship between the indentation force and depth (i.e., $F(d)$) (see Figure 1c) provides a means to extract the mechanical properties of the ultrathin specimen from drumhead nanoindentation measurements. For example, the most widely used formula, the Schwerin-type solution, for extracting the in-plane Young's modulus (E_{2D}) is

$$F = \pi T_{pre} d + \alpha(\nu)\frac{E_{2D}}{a^2} d^3, \tag{1}$$

where $\alpha(\nu) \approx (1.05 - 0.15\nu - 0.16\nu^2)^{-3}$ and ν is Poisson's ratio (Lee et al., 2008). This approximate formula is based on the assumptions of a point load and a fixed edge, where the prestress dominates the small deflections (see the linear term) while membrane elasticity dominates the large deflections (see the cubic term). Using this formula to fit the measured indentation load–deflection curves, researchers extracted E_{2D} and T_{pre} for a specific specimen.

Furthermore, the breaking strength of the material (σ_{2D}^{max}) is determined by measuring the fracture force (F_{max}) and then extracting it using the formula

$$\sigma_{2D}^{max} = \sqrt{\frac{F_{max} E_{2D}}{4\pi R}}. \tag{2}$$

This formula is derived based on the assumptions of a non-adhesive and frictionless spherical tip and a fixed edge (Bhatia and Nachbar, 1968).

However, the estimated values of E_{2D} and σ_{2D}^{max} for the same material (e.g., monolayer graphene) using Eqs. (1) and (2) exhibit diversity (see Table 1 for details). One potential factor contributing to this variability is the influence of adhesive and frictional

Table 1
A summary of geometric and mechanical parameters given by previous drumhead nanoindentation experiments (Bertolazzi et al., 2011; Cooper et al., 2013; Liu et al., 2014; Manzanares-Negro et al., 2021; Sun et al., 2022; Lee et al., 2008, 2013; Suk et al., 2015; López-Polín et al., 2015; Falin et al., 2017). E_{2D} and σ_{2D}^{max} are estimated using Eqs. (1) and (2).

Material	Reference	Drumhead radius (a)	Tip radius (R)	Prestress (T_{pre})	2D Young's modulus (E_{2D})	Fracture force (F_{max})	Maximum 2D stress (σ_{2D}^{max})	Fracture deflection (d_{max})	Fracture strain (ε_{int})
Monolayer MoS_2 ($\nu = 0.27$; $t = 0.65$ nm)	Bertolazzi et al. (2011)	275 nm	12 nm	0.02 – 0.1 N/m	180 ± 60 N/m	172 ± 6 nN	15 ± 3 N/m	~41 nm	6 – 11%
	Cooper et al. (2013)	250 nm	26 nm	0.4 ± 0.2 N/m	120 ± 30 N/m	1500 ± 300 nN	16.5 N/m	~98 nm	/
	Liu et al. (2014)	550 nm	~10 nm	0.11 ± 0.04 N/m	171 ± 11 N/m	/	/	/	/
	Manzanares-Negro et al. (2021)	250 – 1000 nm	20 – 250 nm	/	200 ± 20 N/m	~900 nN	10 ± 1 N/m	~140 nm	/
	Sun et al. (2022)	550 nm	~15 nm	0.08 ± 0.1 N/m	165 ± 45 N/m	/	/	/	/
		750 nm				1420 nN	~35 N/m	~190 nm	/
Monolayer graphene ($\nu = 0.165$; $t = 0.335$ nm)	Lee et al. (2008)	500 nm	16.5 nm	0.07 – 0.74 N/m	342 ± 30 N/m	1770 nN	55 N/m	~116 nm	25%
			27.5 nm			2890 nN		~140 nm	
	Lee et al. (2013)	500/ 750 nm	38 nm	/	324 ± 13 N/m	3410 ± 260 nN	34.5 N/m	/	20%
	Suk et al. (2015)	4500 nm	800 nm	/	/	4650 nN	15.2 ± 3.5 N/m	460 nm	/
			950 nm			1680 nN		600 nm	
	López-Polín et al. (2015)	250 – 1500 nm	60 nm	0.05 – 0.8 N/m	250 – 360 N/m	~1700 – 2100 nN	28 – 35 N/m	/	/
	Falin et al. (2017)	650 nm	6.3 nm	/	342 ± 8 N/m	/	41.9 N/m	/	/

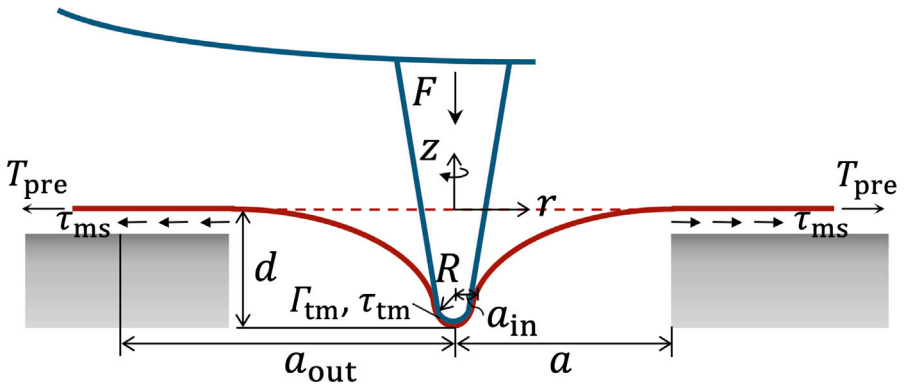


Fig. 2. Cross-sectional sketch of a suspended membrane with prestress being indented by an adhesive and frictional spherical tip of finite radius R, taking into account a sliding edge. The red dashed line indicates the neutral plane of the membrane in its undeformed state.

contacts on these relationships, which are the main focus of this paper. To address this question, we begin by analyzing the force equilibrium in the suspended membrane under indentation. It should be noted that all the parameters discussed throughout this article are based on previous nanoindentation experiments performed on monolayer 2D materials, as documented in Table 1.

3. Model formulation

3.1. Force equilibrium

Figure 2 illustrates the cross-sectional view of the deformed configuration of the suspended membrane, resembling an axisymmetric tent, with a polar coordinate system (r, z) established at the neutral plane of its undeformed configuration. We first define the radial and vertical displacements of an arbitrary material point on the neutral plane as $u(r)$ and $w(r)$, respectively. A stress function $\psi(r)$ is defined such that the radial and hoop 2D membrane stresses are $N_r = \frac{\psi}{r^2}$ and $N_\theta = \frac{\psi'}{r} - \frac{\psi}{r^2}$, respectively. In the suspended region ($r \in [a_{in}, a]$), the out-of-plane force balance and strain compatibility are described by the Föppl–von Kármán (FvK) equations (Mansfield, 2005):

$$\begin{cases} \psi w' - \frac{Fr}{2\pi} = 0 \\ \psi'' - \frac{\psi'}{r} + \frac{E_{2D}}{2} w'^2 = 0 \end{cases} \quad \text{at} \quad r \in [a_{in}, a], \tag{3}$$

where $()'$ denotes $\mathrm{d}()/\mathrm{d}r$. Note that a_{in} is unknown a priori and depends on the adhesive and frictional contacts between the indenter tip and the membrane during the indentation process.

Table 1 summarizes the geometric and mechanical parameters obtained from previous nanoindentation tests on monolayer graphene and MoS_2. Based on the ground, we adopt the conventional assumptions of small deformation ($\epsilon_{\mathrm{int}} \lesssim 0.25$) and moderate central deflection ($d_{\max}/a \lesssim 0.4$) in modeling. Thus, a linear constitutive law is adopted to describe the material behavior, which is

$$\begin{cases} N_r = \frac{E_{2\mathrm{D}}}{1-\nu^2}(\epsilon_r + \nu\epsilon_\theta) \\ N_\theta = \frac{E_{2\mathrm{D}}}{1-\nu^2}(\epsilon_\theta + \nu\epsilon_r) \end{cases}, \tag{4}$$

where ϵ_r and ϵ_θ are radial and hoop membrane strains, respectively. Furthermore, the kinematics of deformation is described by

$$\begin{cases} \epsilon_r = u' + \frac{1}{2}w'^2 \\ \epsilon_\theta = \frac{u}{r} \end{cases}. \tag{5}$$

The in-plane displacement, according to Eqs. (4)–(5), can be expressed in terms of the stress function, which is given by

$$u(r) = \frac{\psi'(r)}{E_{2\mathrm{D}}} - \frac{1+\nu}{E_{2\mathrm{D}}}\frac{\psi(r)}{r}. \tag{6}$$

Now, let us consider the in-plane force equilibrium in the supported region (i.e., $r \in [a, a_{\mathrm{out}}]$) where $w = 0$. This can be represented as (Dai et al., 2018)

$$ru'' + u' - \frac{u}{r} + \frac{(1-\nu^2)\tau_{\mathrm{ms}}}{E_{2\mathrm{D}}}r = 0 \quad \text{at} \quad r \in [a, a_{\mathrm{out}}]. \tag{7}$$

It is crucial to note that a_{out} evolves during indentation and is unknown a priori, satisfying the initial condition that the 2D membrane stresses return to their prestress state at this contact edge (i.e., $N_r(a_{\mathrm{out}}) = N_\theta(a_{\mathrm{out}}) = T_{\mathrm{pre}}$).

We then move on to the contact region (i.e., $r \in [0, a_{\mathrm{in}}]$) where $w(r) = w(0) + R - \sqrt{(R^2 - r^2)} \approx w(0) + \frac{r^2}{2R}$ at $r \ll R$. The in-plane force equilibrium is given by (Dai et al., 2018)

$$ru'' + u' - \frac{u}{r} + \frac{1-\nu}{2}w'^2 + rw'w'' - \frac{(1-\nu^2)\tau_{\mathrm{tm}}}{E_{2\mathrm{D}}}r = 0 \quad \text{at} \quad r \in [0, a_{\mathrm{in}}]. \tag{8}$$

The in-plane equilibrium equations, Eqs. (7) and (8), can be derived from the calculus of variations based on the principle of minimum free energy (see Appendix A for details).

3.2. Boundary conditions at $r = a$

Considering $N_r(a_{\mathrm{out}}) = N_\theta(a_{\mathrm{out}}) = T_{\mathrm{pre}}$, the in-plane displacement at $r \in [a, a_{\mathrm{out}}]$ can be derived from Eq. (7), written as

$$u(r) = \frac{(1-\nu)T_{\mathrm{pre}}}{E_{2\mathrm{D}}}r + \frac{(1-\nu^2)\tau_{\mathrm{ms}}}{E_{2\mathrm{D}}}\left(\frac{a_{\mathrm{out}}r}{2} - \frac{a_{\mathrm{out}}^3}{6r} - \frac{r^2}{3}\right). \tag{9}$$

Furthermore, according to Eqs. (6) and (9), the stress function at $r \in [a, a_{\mathrm{out}}]$ is written as

$$\psi(r) = T_{\mathrm{pre}}r^2 + \tau_{\mathrm{ms}}r^2\left(\frac{1+\nu}{2}a_{\mathrm{out}} + \frac{1-\nu}{6}\frac{a_{\mathrm{out}}^3}{r^2} - \frac{2+\nu}{3}r\right). \tag{10}$$

We consider continuous displacements and 2D membrane stresses in $r = a$, i.e., $[\![u]\!] = [\![w]\!] = [\![N_r]\!] = [\![N_\theta]\!] = 0$, where $[\![f]\!] = f^- - f^+$ (Dai and Lu, 2021). These lead to the following three boundary conditions,

$$\begin{cases} w(a^-) = 0 \\ u(a^-) = \frac{(1-\nu)T_{\mathrm{pre}}}{E_{2\mathrm{D}}}a + \frac{(1-\nu^2)\tau_{\mathrm{ms}}}{E_{2\mathrm{D}}}\left(\frac{a_{\mathrm{out}}a}{2} - \frac{a_{\mathrm{out}}^3}{6a} - \frac{a^2}{3}\right), \\ N_r(a^-) = T_{\mathrm{pre}} + \tau_{\mathrm{ms}}\left(\frac{1+\nu}{2}a_{\mathrm{out}} + \frac{1-\nu}{6}\frac{a_{\mathrm{out}}^3}{a^2} - \frac{2+\nu}{3}a\right), \end{cases} \tag{11}$$

where a^- indicates the inner side of $r = a$.

As $\tau_{\mathrm{ms}} \to \infty$, $a_{\mathrm{out}} \to a$, and the sliding edge between the membrane and the supporting substrate behaves as a fixed one, so that Eq. (11) simplifies to

$$\begin{cases} w(a^-) = 0 \\ u(a^-) = \frac{(1-\nu)T_{\mathrm{pre}}}{E_{2\mathrm{D}}}a \end{cases}. \tag{12}$$

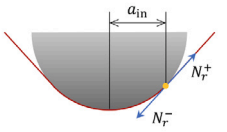
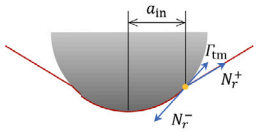
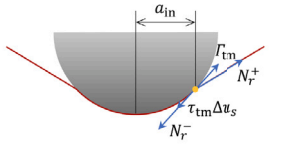
The force continuity condition, part of Eq. (11), is omitted since the displacement at the contact line (i.e., $r = a$) is prescribed (Majidi and Adams, 2009).

As $\tau_{\mathrm{ms}} \to 0$, the edge behaves as a frictionless one, and Eq. (11) simplifies to (Rao et al., 2023)

$$\begin{cases} w(a^-) = 0 \\ N_r(a^-) + N_\theta(a^-) = 2T_{\mathrm{pre}} \end{cases}, \tag{13}$$

as the displacement and force continuities are both preserved across $r = a$.

Table 2
Illustration of force balances at the contact line (yellow dots) between the spherical tip and the indented membrane with three different boundary conditions at $r = a_{in}$. N_r^- and N_r^+ represent the radial 2D membrane stress at the inner and outer sides of the contact line, respectively.

Contact type	Non-adhesive & frictionless	Adhesive & frictionless	Adhesive & frictional
Schematic			
Continuity	$[\![u]\!] = [\![w]\!] = [\![N_r]\!] = [\![N_\theta]\!] = 0$ at $r = a_{in}$		
Boundary condition	$\begin{cases} \psi(a_{in}^+) = \frac{FR}{2\pi} \\ \frac{2\psi(a_{in}^+)}{a_{in}^2} - \frac{\psi'(a_{in}^+)}{a_{in}} = \frac{E_{2D}a_{in}^2}{8R^2} \end{cases}$	$\begin{cases} \frac{1}{2R^2\psi(a_{in}^+)}\left[\psi(a_{in}^+) - \frac{FR}{2\pi}\right]^2 = \Gamma_{tm} \\ \frac{2\psi(a_{in}^+)}{a_{in}^2} - \frac{\psi'(a_{in}^+)}{a_{in}} = \frac{E_{2D}a_{in}^2}{8R^2} \end{cases}$	$\begin{cases} \frac{1}{2R^2\psi(a_{in}^+)}\left[\psi(a_{in}^+) - \frac{FR}{2\pi}\right]^2 = \Gamma_{tm} - \tau_{tm}\Delta u_s \\ \frac{2\psi(a_{in}^+)}{a_{in}^2} - \frac{\psi'(a_{in}^+)}{a_{in}} = \frac{E_{2D}a_{in}^2}{8R^2} + \frac{(1-\nu)\tau_{tm}a_{in}}{3} \end{cases}$
Controlling parameter	$\mathcal{R}_s = \frac{R}{a}\sqrt{\frac{T_{pre}}{E_{2D}}}$	$\mathcal{R}_s = \frac{R}{a}\sqrt{\frac{T_{pre}}{E_{2D}}};\ \mathcal{A} = \frac{\Gamma_{tm}E_{2D}}{T_{pre}^2}$	$\mathcal{R}_s = \frac{R}{a}\sqrt{\frac{T_{pre}}{E_{2D}}};\ \mathcal{A} = \frac{\Gamma_{tm}E_{2D}}{T_{pre}^2};\ \mathcal{K} = \frac{\tau_{tm}a}{T_{pre}}$

3.3. Boundary conditions at $r = a_{in}$

Considering $u(0) = 0$ due to the axisymmetry, the in-plane displacement at $r \in [0, a_{in}]$ can be derived from Eq. (8), written as

$$u(r) = Cr - \frac{3-\nu}{16R^2}r^3 + \frac{(1-\nu^2)\tau_{tm}}{3E_{2D}}r^2, \tag{14}$$

where C is an unknown constant. Therefore, according to Eqs. (6) and (14), the stress function at $r \in [0, a_{in}]$ is written as

$$\psi(r) = \frac{E_{2D}}{1-\nu}Cr^2 - \frac{E_{2D}}{16R^2}r^4 + \frac{2+\nu}{3}\tau_{tm}r^3. \tag{15}$$

When considering a non-adhesive and frictionless tip (i.e., $\Gamma_{tm} = \tau_{tm} = 0$), there are continuous displacements and 2D membrane stresses across $r = a_{in}$, i.e., $[\![u]\!] = [\![w]\!] = [\![N_r]\!] = [\![N_\theta]\!] = 0$ (Majidi and Adams, 2009). These lead to the following two boundary conditions,

$$\begin{cases} \psi(a_{in}^+) = \frac{FR}{2\pi} \\ \frac{2\psi(a_{in}^+)}{a_{in}^2} - \frac{\psi'(a_{in}^+)}{a_{in}} = \frac{E_{2D}a_{in}^2}{8R^2} \end{cases}, \tag{16}$$

where a_{in}^+ indicates the outer side of $r = a_{in}$. The same boundary conditions are observed in Chandler and Vella (2020). In particular, the second equation of Eq. (16) represents membrane tension continuity across $r = a_{in}$, which is obtained from $[\![N_r - N_\theta]\!]_{r=a_{in}} = 0$ with the aid of Eqs. (14) and (15). According to the force balance at the contact line (see the force balance diagram provided in the first column of Table 2), there is a continuous slope across $r = a_{in}$, as represented by the first equation of Eq. (16).

When considering an adhesive and frictionless tip (i.e., $\Gamma_{tm} \neq 0$ & $\tau_{tm} = 0$), the boundary conditions at $r = a_{in}$ are expressed as

$$\begin{cases} \frac{[\psi(a_{in}^+) - \frac{FR}{2\pi}]^2}{2R^2\psi(a_{in}^+)} = \Gamma_{tm} \\ \frac{2\psi(a_{in}^+)}{a_{in}^2} - \frac{\psi'(a_{in}^+)}{a_{in}} = \frac{E_{2D}a_{in}^2}{8R^2} \end{cases}. \tag{17}$$

The upper equation implies a slope jump across $r = a_{in}$ induced by the adhesion energy (Γ_{tm}) at the tip-membrane interface, resulting in a tangential force balance at the contact line, as depicted in the second column of Table 2. The same force balance at the contact line for bulging (inverse indentation under pressure) can be found in Rao et al. (2021), validating the findings.

When considering an adhesive and frictional tip (i.e., $\Gamma_{tm} \neq 0$ & $\tau_{tm} \neq 0$), the boundary conditions are expressed as

$$\begin{cases} \frac{[\psi(a_{in}^+) - \frac{FR}{2\pi}]^2}{2R^2\psi(a_{in}^+)} = \Gamma_{tm} - \tau_{tm}\Delta u_s \\ \frac{2\psi(a_{in}^+)}{a_{in}^2} - \frac{\psi'(a_{in}^+)}{a_{in}} = \frac{E_{2D}a_{in}^2}{8R^2} + \frac{(1-\nu)\tau_{tm}a_{in}}{3} \end{cases}, \tag{18}$$

Where $\Delta u_s = u(a_{\text{in}}) - \frac{(1-\nu)T_{\text{pre}}}{E_{\text{2D}}} a_{\text{in}}$ represents the difference in radial displacement at $r = a_{\text{in}}$, compared to a reference state where the membrane fully sticks to the tip during indentation. Although the indentation process modifies the radial displacement below the tip, this modification is minor and independent of the indentation depth, as has been demonstrated in the indentation of a half space (Zhupanska, 2009; Borodich et al., 2014). Therefore, we neglect this modification and preserve radial displacement induced by prestress (i.e., $u(r) = \frac{(1-\nu)T_{\text{pre}}}{E_{\text{2D}}} r$), within the range of $r \in [0, a_{\text{in}}]$ for the full stick case, considering experimental observations for small deformation and small tip size (see Table 1 for details). As seen in the third column of Table 2, the adhesive and shear forces at the tip-membrane interface play contrasting roles in the force balance at the tip-membrane contact line: adhesion facilitates the slope jump, while friction prohibits it.

When considering an adhesive and non-slip tip (i.e., $\Gamma_{\text{tm}} \neq 0$ & $\tau_{\text{tm}} \to \infty$), the boundary conditions are expressed as

$$\begin{cases} \frac{[\psi(a_{\text{in}}^+) - \frac{FR}{2\pi}]^2}{2R^2\psi(a_{\text{in}}^+)} + \frac{(1-\nu^2)}{2E_{\text{2D}}}\left[\frac{\psi(a_{\text{in}}^+)}{a_{\text{in}}^2} - T_{\text{pre}} - \frac{E_{\text{2D}}a_{\text{in}}^2}{2(1-\nu^2)R^2}\right]^2 = \Gamma_{\text{tm}} \\ \frac{\psi'(a_{\text{in}}^+)}{E_{\text{2D}}} - \frac{(1+\nu)\psi(a_{\text{in}}^+)}{E_{\text{2D}}a_{\text{in}}} = \frac{(1-\nu)T_{\text{pre}}a_{\text{in}}}{E_{\text{2D}}} \end{cases}. \tag{19}$$

The upper equation implies a discontinuity of radial membrane stress across the tip-membrane contact line due to the non-slip condition, similar to what occurs at the contact line during bulging (Rao et al., 2021). This equation provides the upper bound of the friction effects on nanoindentation and can also be derived using approaches in fracture mechanics, such as the J-integral method (Majidi and Adams, 2009; Lee et al., 2018). The lower equation suggests a continuity of radial displacement across the contact line.

The derivation of the boundary equations in this subsection, using an energy approach, is detailed in Appendix A.

4. Numerical implementation

We introduce nondimensionalization below to facilitate the numerical solutions for the BVPs organized in this paper. A characteristic length in the vertical direction, $L = \sqrt{T_{\text{pre}}/E_{\text{2D}}}a$, is then identified here, which leads to

$$\begin{aligned} &\rho = \frac{r}{a}, \rho_{\text{in}} = \frac{a_{\text{in}}}{a}, \rho_{\text{o}} = \frac{a_{\text{out}}}{a}, U = \frac{u}{a}, \delta = \frac{d}{L}, W = \frac{w}{L}, \\ &\mathcal{F} = \frac{F}{T_{\text{pre}}L}, \bar{\psi} = \frac{\psi}{T_{\text{pre}}a^2}, \mathcal{N}_r = \frac{N_r}{T_{\text{pre}}}, \mathcal{N}_\theta = \frac{N_\theta}{T_{\text{pre}}}, \\ &\mathcal{R}_{\text{s}} = \frac{RL}{a^2}, \mathcal{A} = \frac{\Gamma_{\text{tm}}E_{\text{2D}}}{T_{\text{pre}}^2}, \mathcal{K} = \frac{\tau_{\text{tm}}a}{T_{\text{pre}}}, \mathcal{T} = \frac{\tau_{\text{ms}}a}{T_{\text{pre}}}, \end{aligned} \tag{20}$$

where $\mathcal{R}_{\text{s}}$ is the dimensionless radius of the spherical tip, $\mathcal{A}$ and $\mathcal{K}$ are the adhesion and friction numbers at the tip-membrane interface, respectively; and $\mathcal{T}$ is the shear number at the membrane-substrate interface. These controlling parameters govern the indentation load–deflection relationship when considering the effects of adhesive and frictional contacts.

According to Eq. (20), the governing equations in the suspended region ($r \in [a_{\text{in}}, a]$), Eq. (3), are rewritten as

$$\begin{cases} \bar{\psi}W' - \frac{\mathcal{F}\rho}{2\pi} = 0 \\ \bar{\psi}'' - \frac{\bar{\psi}'}{\rho} + \frac{W'^2}{2} = 0 \end{cases} \quad \text{at} \quad \rho \in [\rho_{\text{in}}, 1]. \tag{21}$$

Five boundary conditions are required to solve this equation numerically since ρ_{in} and ρ_{o} are unknown parameters a priori.

According to Eqs. (6), (11), and (20), the sliding boundary conditions at $\rho = 1$ are given by

$$\begin{cases} W(1) = 0 \\ \bar{\psi}'(1) - (1+\nu)\bar{\psi}(1) = 1 - \nu + (1-\nu^2)\mathcal{T}(\frac{\rho_{\text{o}}}{2} - \frac{\rho_{\text{o}}^3}{6} - \frac{1}{3}) \\ \bar{\psi}(1) = 1 + \mathcal{T}(\frac{1+\nu}{2}\rho_{\text{o}} + \frac{1-\nu}{6}\rho_{\text{o}}^3 - \frac{2+\nu}{3}) \end{cases}. \tag{22}$$

We further consider two limiting cases of the boundary condition at $\rho = 1$: the fixed edge with boundary conditions given in Eq. (12), which can be rewritten as

$$\begin{cases} W(1) = 0 \\ \bar{\psi}'(1) - (1+\nu)\bar{\psi}(1) = 1 - \nu \end{cases}; \tag{23}$$

the frictionless edge with boundary conditions given in Eq. (13), which can be rewritten as

$$\begin{cases} W(1) = 0 \\ \bar{\psi}'(1) = 2 \end{cases}. \tag{24}$$

To formulate the closed form of the BVP relevant to the assumption of the non-adhesive and frictionless tip, we rewrite the two additional boundary conditions at $\rho = \rho_{\text{in}}$, given by Eq. (16), as

$$\begin{cases} \bar{\psi}(\rho_{\text{in}}) = \frac{\mathcal{F}\mathcal{R}_{\text{s}}}{2\pi} \\ 2\bar{\psi}(\rho_{\text{in}}) - \rho_{\text{in}}\bar{\psi}'(\rho_{\text{in}}) = \frac{\rho_{\text{in}}^4}{8\mathcal{R}_{\text{s}}^2} \end{cases}. \tag{25}$$

Table 3
A summary of controlling parameters identified by our model but obtained from previous drumhead nanoindentation experiments or simulations. The pink-highlighted columns, which relate to adhesion and friction numbers, are assessed using vdW interactions, while the green columns are based on chemical bonds (Bertolazzi et al., 2011; Cooper et al., 2013; Liu et al., 2014; Manzanares-Negro et al., 2021; Sun et al., 2022; Lee et al., 2008, 2013; Suk et al., 2015; López-Polín et al., 2015; Falin et al., 2017; Kumar and Parks, 2015).

Material	Reference	$\frac{R}{a}$	$\frac{L}{a}=\sqrt{\frac{T_{pre}}{E_{2D}}}$	$\mathcal{R}_s=\frac{RL}{a^2}$	$\delta_{max}=\frac{d_{max}}{L}$	$\mathcal{F}_{max}=\frac{F_{max}}{T_{pre}L}$	$\mathcal{A}=\frac{\Gamma_{tm}E_{2D}}{T_{pre}^2}$		$\mathcal{K}=\frac{\tau_{tm}a}{T_{pre}}$		$\mathcal{T}=\frac{\tau_{ms}a}{T_{pre}}$
Monolayer MoS_2	Bertolazzi et al. (2011)	0.04	0.011 – 0.024	0.0004 – 0.001	6 – 14	261 – 2843	9e3 – 2e5	5e4 – 1e6	30 – 90	8e4 – 4e5	30 – 152
	Cooper et al. (2013)	0.1	0.058	0.0058	6.76	259	372	2e3	4	1.8e4	7
	Liu et al. (2014)	0.02	0.025	0.0005	/	/	7e3	4e4	33	1.4e5	55
	Manzanares-Negro et al. (2021)	0.08 – 0.25	/	/	/	/	/	/	/	/	/
	Sun et al. (2022)	0.03	0.021	0.0006	/	/	1.5e4	7.6e4	81	2e5	81
		0.02	0.021	0.0004	12	1183			111	2.8e5	111
Monolayer graphene	Lee et al. (2008)	0.03	0.014 – 0.047	0.0004 – 0.001	5 – 17	102 – 3612	3e2 – 3.6e4	2e3 – 2e5	4 – 47	2e4 – 2e5	1 – 12
		0.06	0.014 – 0.047	0.0008 – 0.003	6 – 20	166 – 5898	3e2 – 3.5e4	2e3 – 2e5	4 – 47	2e4 – 2e5	1 – 12
	Lee et al. (2013)	0.05 /0.08	/	/	/	/	/	/	/	/	/
	Suk et al. (2015)	0.18 – 0.21	/	/	/	/	/	/	/	/	/
	López-Polín et al. (2015)	0.04 – 0.24	0.012 – 0.057	0.00048 – 0.014	/	25 – 14000	192 – 7e4	1e3 – 3.6e5	2 – 197	9e3 – 8.5e5	0.5 – 49
	Falin et al. (2017)	0.01	/	/	/	/	/	/	/	/	/

Similarly, to formulate the closed form of the BVP relevant to the assumption of adhesive and frictionless tip, we rewrite the two additional boundary conditions at $\rho=\rho_{in}$, given by Eq. (17), as

$$\begin{cases}(\bar{\psi}(\rho_{in})-\frac{\mathcal{F}\mathcal{R}_s}{2\pi})^2=2\mathcal{A}\mathcal{R}_s^2\bar{\psi}(\rho_{in})\\ 2\bar{\psi}(\rho_{in})-\rho_{in}\bar{\psi}'(\rho_{in})=\frac{\rho_{in}^4}{8\mathcal{R}_s^2}\end{cases}. \tag{26}$$

Notably, it simplifies to Eq. (25) when $\mathcal{A}=0$.

To formulate the closed form of the BVP relevant to the assumption of adhesive and frictional tip, we rewrite the two additional boundary conditions at $\rho=\rho_{in}$, given by Eq. (18), as

$$\begin{cases}(\bar{\psi}(\rho_{in})-\frac{\mathcal{F}\mathcal{R}_s}{2\pi})^2=2\mathcal{R}_s^2\bar{\psi}(\rho_{in})[\mathcal{A}-\mathcal{K}(\bar{\psi}'(\rho_{in})-(1+\nu)\frac{\bar{\psi}(\rho_{in})}{\rho_{in}}-(1-\nu)\rho_{in})]\\ 2\bar{\psi}(\rho_{in})-\rho_{in}\bar{\psi}'(\rho_{in})=\frac{\rho_{in}^4}{8\mathcal{R}_s^2}+\frac{(1-\nu)\mathcal{K}\rho_{in}^3}{3}\end{cases}. \tag{27}$$

Notably, it simplifies to Eq. (26) when $\mathcal{K}=0$, and further simplifies to Eq. (25) when $\mathcal{A}=0$ and $\mathcal{K}=0$.

Finally, to formulate the closed form of the BVP relevant to the adhesive and non-slip tip assumption, we rewrite the two additional boundary conditions at $\rho=\rho_{in}$, given by Eq. (19), as

$$\begin{cases}\frac{(\bar{\psi}(\rho_{in})-\frac{\mathcal{F}\mathcal{R}_s}{2\pi})^2}{2\mathcal{R}_s^2\bar{\psi}(\rho_{in})}+\frac{1-\nu^2}{2}(\frac{\bar{\psi}(\rho_{in})}{\rho_{in}^2}-1-\frac{\rho_{in}^2}{2(1-\nu^2)\mathcal{R}_s^2})^2=\mathcal{A}\\ \bar{\psi}'(\rho_{in})-(1+\nu)\frac{\bar{\psi}(\rho_{in})}{\rho_{in}}=(1-\nu)\rho_{in}\end{cases}. \tag{28}$$

All the BVPs formulated above are numerically solved using the BVP4C package in MATLAB.

5. Results and discussions

The relevant controlling parameters for this study, as determined by previous drumhead nanoindentation experiments, are summarized in Table 3. The range of these values will guide the subsequent numerical studies and discussions. Additionally, we adopt Poisson's ratio of monolayer graphene (e.g., $\nu=0.165$) in what follows as a demonstration.

5.1. Effects of the tip/membrane adhesion

Fig. 3a presents the numerical results for the dimensionless indentation load–deflection relationship derived from the model with an adhesive and frictionless spherical tip, along with a fixed edge between the membrane and the substrate (i.e., numerical solutions to the BVP given by Eqs. (21), (23), and (26)). The results cover a range of assumed sphere radii and adhesion numbers, with the

typical maximal indentation depth used in previous drumhead nanoindentation experiments indicated (see Table 3 for details). Notably, when the adhesive forces between the tip and the membrane are considered, a significant observation emerges: the load–deflection relationship exhibits instabilities. These instabilities manifest as approaching spherical tips "jumping in" to contact, while separated tips "jump out" at a "pull-off force" (see dashed curves in Fig. 3a). This behavior differs from the model with non-adhesive and frictionless spherical tips (exhibited by solid curves in Fig. 3a) but aligns with previous experimental observations (Lee et al., 2008; Rokni and Lu, 2020). However, discussing these instabilities under force control falls beyond the scope of this paper and will be explored in future research. This paper focuses on drumhead nanoindentation under displacement control, starting from $\delta = 0$ with an initial negative (upward) force.

In Fig. 3b, we depict the force discrepancy between an adhesive tip case (i.e., $\mathcal{F}_{\mathcal{A}}$ when $\mathcal{A} = 10^4$) and a non-adhesive tip case (i.e., $\mathcal{F}$ when $\mathcal{A} = 0$) at the same indentation depth. Specifically, we define the force discrepancy as $\mathrm{Discr} = |1 - \mathcal{F}_{\mathcal{A}}/\mathcal{F}|$. We observe that the force discrepancy decreases as the indentation depth increases. The reduced impact of tip/membrane adhesion on the load–deflection relationship is further confirmed by the convergence of numerical solutions for the two scenarios at large deflections, as shown in Supplementary Fig. B.1. Meanwhile, the force discrepancy also decreases as the tip size shrinks. This observation suggests that to mitigate undesired adhesive effects when extracting $E_{2\mathrm{D}}$ by fitting measured load–deflection curves using Eq. (1), we should select smaller tip sizes (e.g., $\mathcal{R}_{\mathrm{s}} \lesssim 10^{-3}$) during testing. Furthermore, numerical studies suggest that excluding measurement data with $\delta \leq 1$ also effectively reduces the influence of tip/membrane adhesion on the load–deflection relationship, with $\mathrm{Discr} \leq 10\%$ observed for most tip sizes and adhesion numbers involved in experiments (see Supplementary Fig. B.2).

In addition to studying the indentation load–deflection relationship, understanding the influence of tip/membrane adhesion on membrane stress is crucial for thin membrane strain engineering and determining breaking strengths. Figure 4 displays dimensionless radial and hoop 2D membrane stress distributions, along with normalized profiles of the indented membrane near the spherical tip, under various $\mathcal{A}$ when $\mathcal{R}_{\mathrm{s}} = 10^{-3}$. The adhesive effect notably increases the maximum 2D membrane stress (which consistently occurs in the center of the suspended membrane), particularly at intermediate indentation depths (e.g. $\delta = 5$), and this influence diminishes as δ increases. This trend is confirmed by the decrease in the discrepancy in the maximum 2D membrane stresses between the adhesive and non-adhesive tip cases with increasing δ, as illustrated in Supplementary Fig. B.3.

In Fig. 5, we present the relative error resulting from the use of Eq. (2) instead of the numerically determined maximum 2D membrane stress, to estimate the breaking strength of the material. Specifically, we define the relative error as $\mathrm{Err} = |1 - \sqrt{\mathcal{F}_{\max}/4\pi\mathcal{R}_{\mathrm{s}}}/\mathcal{N}_{2\mathrm{D}}^{\max}|$, where $\mathcal{N}_{2\mathrm{D}}^{\max}$ is the numerically obtained maximum 2D membrane stress under $\mathcal{F}_{\max}$. We observe that within the experimental range, the error of the adhesive tip case is larger than that of the non-adhesive tip case, regardless of the tip size, and it decreases as the tip size decreases for both cases. Therefore, we conclude that a sharper tip provides a better prediction of the breaking strength using Eq. (2).

Figure 5b and c display the lower thresholds of the desired indentation depth before rupture, which account for the adhesive forces between the tip and the membrane, to ensure that the error remains within 10% and 5%, respectively. We observe that these thresholds are comparable to the maximum indentation depth measured in the experiments (see Table 3 for details). Therefore, for enhanced accuracy in determining the breaking strength of the material via drumhead nanoindentation, future research should explore new formulations that consider tip-membrane interfacial interactions, rather than rely solely on Eq. (2).

5.2. Effects of an adhesive and frictional spherical tip

In addition to the scenario characterized by vdW interactions at the tip-membrane interface (see Section 5.1), where relatively large normal tractions and negligible tangential tractions are observed, the frictional behavior becomes particularly intriguing in scenarios where chemical bonds coexists alongside vdW interactions at this interface (refer to Table 3 for details) (Kumar and Parks, 2015).

Figure 6 presents the numerical results for the dimensionless indentation load–deflection relationship obtained from the model featuring an adhesive and frictional spherical tip, along with a fixed edge (i.e., numerical solutions to the BVP given by Eqs. (21), (23), and (27)). We set the dimensionless radius of the sphere as $\mathcal{R}_{\mathrm{s}} = 10^{-3}$ and the adhesion number as $\mathcal{A} = 10^5$, while varying the friction number $\mathcal{K}$ across four orders of magnitude to incorporate both lubricant and stick tip-membrane interfaces. Additionally, the numerical solutions for two limiting cases, a frictionless tip (i.e., $\mathcal{K} \to 0$, for the BVP given by Eqs. (21), (23), and (27)) and a non-slip tip (i.e., $\mathcal{K} \to \infty$, for the BVP given by Eqs. (21), (23), and (28)), are presented in the same figure. Comparison of these numerical results reveals that indenting a lubricated membrane is slightly easier than indenting a sticky membrane to the same indentation depth. Furthermore, this discrepancy diminishes as the tip size shrinks, as validated by the convergence of numerical solutions at $\mathcal{K} \to 0$ and $\mathcal{K} \to \infty$ when $\mathcal{R}_{\mathrm{s}} = 10^{-5}$ (see Supplementary Fig. B.4).

In Fig. 7, the distribution of dimensionless radial and hoop 2D membrane stresses is illustrated, along with normalized profiles of the indented membrane near the spherical tip. Notably, compared to the non-adhesive and frictionless tip, the adhesive and frictional tip induces a compressive zone along the hoop direction near the contact line between the tip and the membrane (see Fig. 7a) at an intermediate deflection (e.g., $\delta = 5$). Because ultrathin membranes barely sustain compressive stresses, we anticipate the occurrence of radial wrinkles across the tip-membrane contact lines due to their adhesive and frictional contacts. As the indentation depth increases, the effects of an adhesive and frictional tip on the distribution of membrane stress diminish, as evident in Fig. 7b. However, a significant observation, differing from the previous cases of adhesive or non-adhesive but frictionless tips, is that the position of the maximum 2D membrane stress is no longer at the center of the suspended membrane but shifts to the contact line between the tip and the membrane. To confirm this, we plot the radial 2D membrane stresses at both $r = 0$ (denoted as $\mathcal{N}_{2\mathrm{D}}^{\mathrm{tc}}$) and $r = a_{\mathrm{in}}$ (denoted as $\mathcal{N}_{2\mathrm{D}}^{\mathrm{te}}$) in Fig. 8. As shown, $\mathcal{N}_{2\mathrm{D}}^{\mathrm{te}} < \mathcal{N}_{2\mathrm{D}}^{\mathrm{tc}}$ at small $\mathcal{K}$ regardless of the indentation depth, while $\mathcal{N}_{2\mathrm{D}}^{\mathrm{te}} > \mathcal{N}_{2\mathrm{D}}^{\mathrm{tc}}$ at

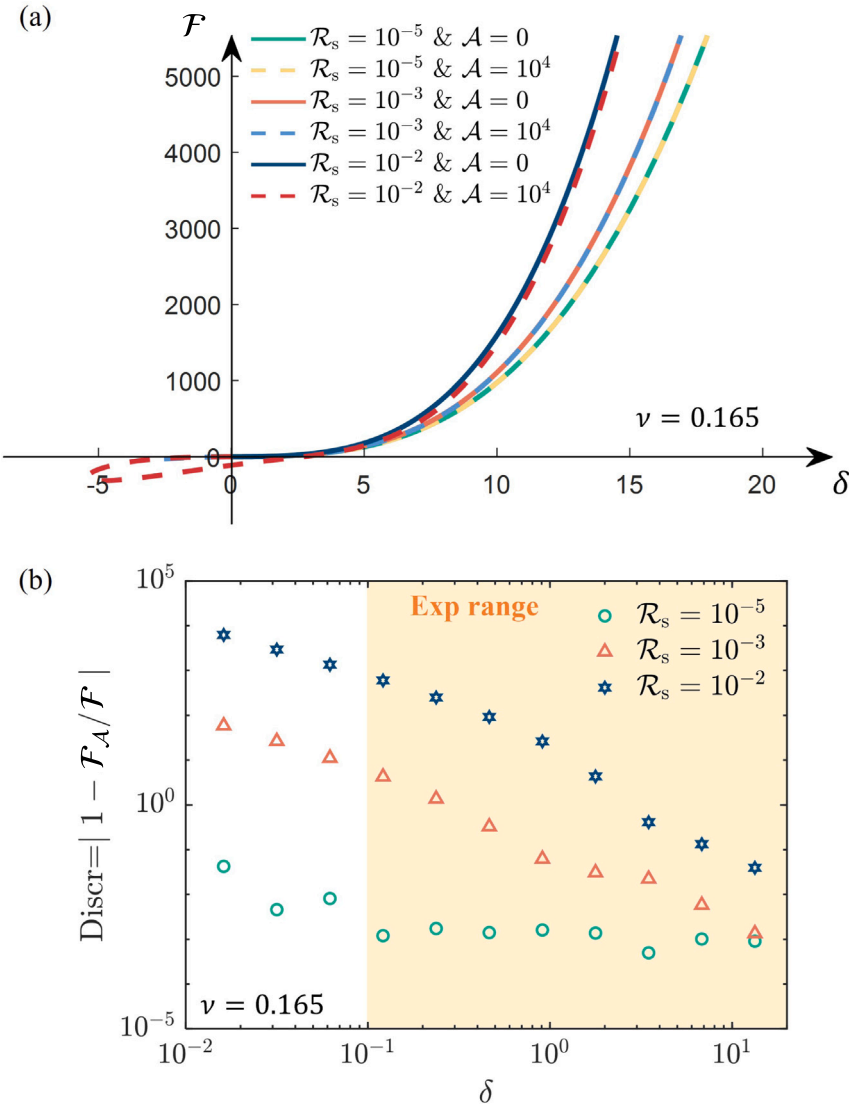


Fig. 3. (a) $\mathcal{F}$ vs. δ under various dimensionless sphere radii ($\mathcal{R}_s$) and adhesion numbers ($\mathcal{A}$). (b) The force discrepancy (Discr) between the adhesive tip case (i.e., $\mathcal{F}_{\mathcal{A}}$ when $\mathcal{A} = 10^4$) and the non-adhesive tip case (i.e., $\mathcal{F}$ when $\mathcal{A} = 0$) at the same indentation depth.

large $\mathcal{K}$. Therefore, our prediction suggests that membrane breakage is more likely to occur in the center of a lubricated membrane, whereas in the case of a sticky membrane, it is more probable to occur in the peripheral region between the tip and the membrane contacts as the indentation depth increases. A similar observation has been previously reported by simulation studies (Kumar and Parks, 2015).

The vdW interactions are the most universal interactions present at the tip-membrane interface, which has been shown to have a slight influence on the indentation load–deflection relationship and maximum 2D membrane stress, according to the numerical analysis above. Therefore, in the following subsection, we assume a non-adhesive and frictionless spherical tip of finite radius and focus on investigating the sliding behavior of the membrane against the supporting substrate during drumhead nanoindentation.

5.3. Effects of a sliding edge

In their study, Chandler and Vella (2020) provided asymptotic expressions for drumhead nanoindentation at small deflections employing a non-adhesive and frictionless spherical tip of finite radius, alongside a fixed edge. These formulas are represented as

$$\frac{\delta}{\mathcal{F}} \sim \begin{cases} \frac{1}{2\pi}\log\sqrt{\frac{2\pi e}{\mathcal{R}_s \mathcal{F}}} & \text{when} \quad \mathcal{F} \ll \mathcal{R}_s \ll 1 \\ \frac{1}{2\pi}\log\frac{8\pi}{\mathcal{F}} & \text{when} \quad \mathcal{R}_s \ll \mathcal{F} \ll 1 \end{cases}. \tag{29}$$

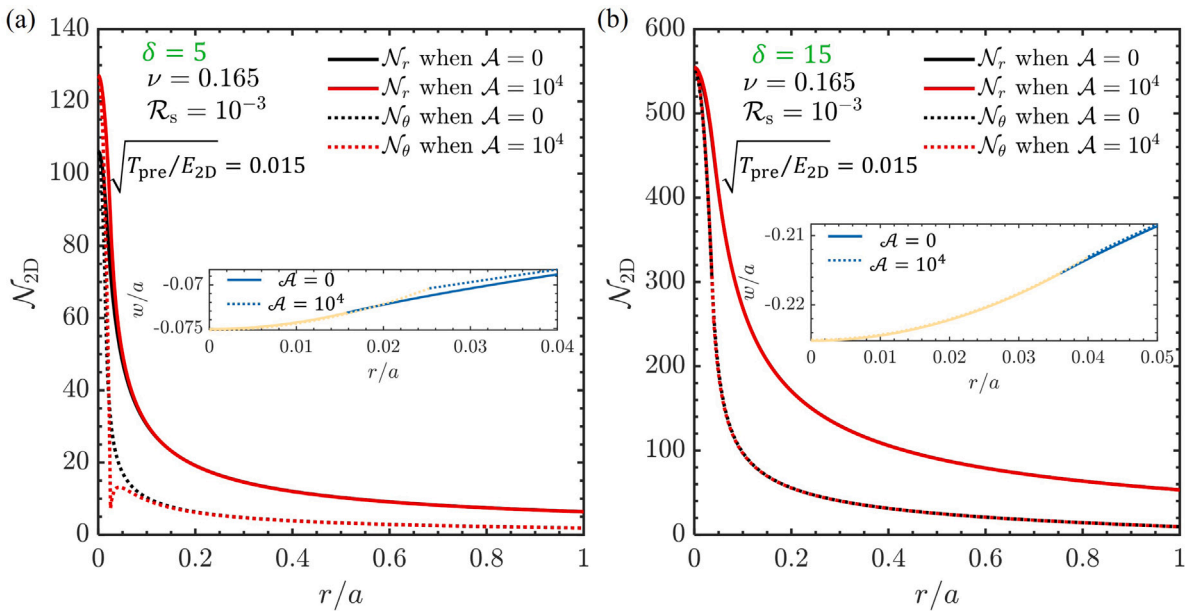


Fig. 4. The dimensionless radial and hoop membrane stress distributions at (a) $\delta = 5$ and (b) $\delta = 15$, respectively, for varying $\mathcal{A}$ when $\mathcal{R}_s = 10^{-3}$. Inset: The corresponding normalized profiles of the indented membrane near the spherical tip. The yellow and blue colors indicate the contact and noncontact regions, respectively.

Figure 9a compares the numerical solutions for the model with a sliding edge (i.e., the BVP given by Eqs. (21), (22), and (25)) under various shear numbers $\mathcal{T}$ to this asymptote within the range of $\mathcal{F} \ll \mathcal{R}_s \ll 1$. The figure illustrates that, despite employing spherical tips with different radii for indentation, the numerical results consistently converge to the asymptote at small indentations. This implies that the indentation load–deflection behavior at the small deflection remains consistent, regardless of the fixed or sliding interface between the membrane and the supporting substrate.

Figure 9b further demonstrates the agreement of the numerical results under various $\mathcal{R}_s$ and $\mathcal{T}$ with the asymptote within the range of $\mathcal{R}_s \ll \mathcal{F} \ll 1$. Consequently, it is deduced that the load–deflection relationship at small indentations remains unaffected by varying shear resistances at the membrane-substrate interfaces. Additionally, the linear compliance (i.e., $\delta/\mathcal{F}$) at small indentations depends on the tip size, where the system is dominated by the effect of tip size, followed by a phase independent of tip size where the system is dominated by prestress. Overall, instead of the linear term given by the widely used formulation in Eq. (1), the load–deflection relationship is nonlinear in the initial phase of tent formation.

Figure 9 suggests that adopting a linear F-d relationship is doomed to fail to accurately capture the small indentation behaviors. For practical purposes, instead of using the logarithmic form in Eq. (29), we perform a power law fitting of the numerical results within the purple regime in Fig. 9b to describe these behaviors. We vary $\mathcal{R}_s$ and $\mathcal{T}$ to capture the experimental range (see Table 3 for details). The least squares fitting yields the following approximate load–deflection relationship at small indentations (i.e., $\mathcal{O}(10^{-1}) \lesssim \mathcal{F} \lesssim \mathcal{O}(1)$)

$$\mathcal{F} \approx 2\delta^{1.2}. \tag{30}$$

As shown in Fig. 9b, this approximate formula closely matches the numerical solutions for small indentations across various experimentally relevant $\mathcal{R}_s$ and $\mathcal{T}$. Finally, the good agreement between our numerical results and the asymptotes provided by previous research validates the accuracy of numerical calculations.

Chandler and Vella (2020) also presented the asymptote for large indentations (i.e., $\mathcal{F} \gg 1$) with a fixed edge. Additionally, Dai and Lu (2021) presented another asymptote for large indentations at the limit of a frictionless edge. Based on their work, we infer the asymptote at large indentations, considering both the fixed and the frictionless edge limits, as

$$\frac{\delta}{\mathcal{F}^{1/3}} \sim \begin{cases} 1.05 - 0.15\nu - 0.16\nu^2 - \frac{2(\sqrt{2}-1)}{\sqrt{\pi}}\sqrt{\mathcal{R}_s\mathcal{F}^{1/3}} & \text{when} \quad \mathcal{T} \to \infty \\ (\frac{\pi}{2})^{1/3} - \frac{2(\sqrt{2}-1)}{\sqrt{\pi}}\sqrt{\mathcal{R}_s\mathcal{F}^{1/3}} & \text{when} \quad \mathcal{T} \to 0 \end{cases}. \tag{31}$$

Figure 10a compares the numerical solutions at $\mathcal{T} \to \infty$ (i.e., solutions for the BVP given by Eqs. (21), (23), and (25)), and at $\mathcal{T} \to 0$ (i.e., solutions for the BVP given by Eqs. (21), (24), and (25)) with these asymptotes. The good agreement validates our inference to establish the asymptotic formulation Eq. (31) and underscores the accuracy of our numerical calculations.

Figure 10b illustrates the dependence of cubic compliance ($\delta/\mathcal{F}^{1/3}$) on $\mathcal{R}_s\mathcal{F}^{1/3}$ under varying $\mathcal{T}$ when $\mathcal{R}_s = 10^{-3}$. In particular, as $\mathcal{T}$ decreases, there is a transition in the load–deflection behavior at large indentations from the asymptote at $\mathcal{T} \to \infty$ to the asymptote

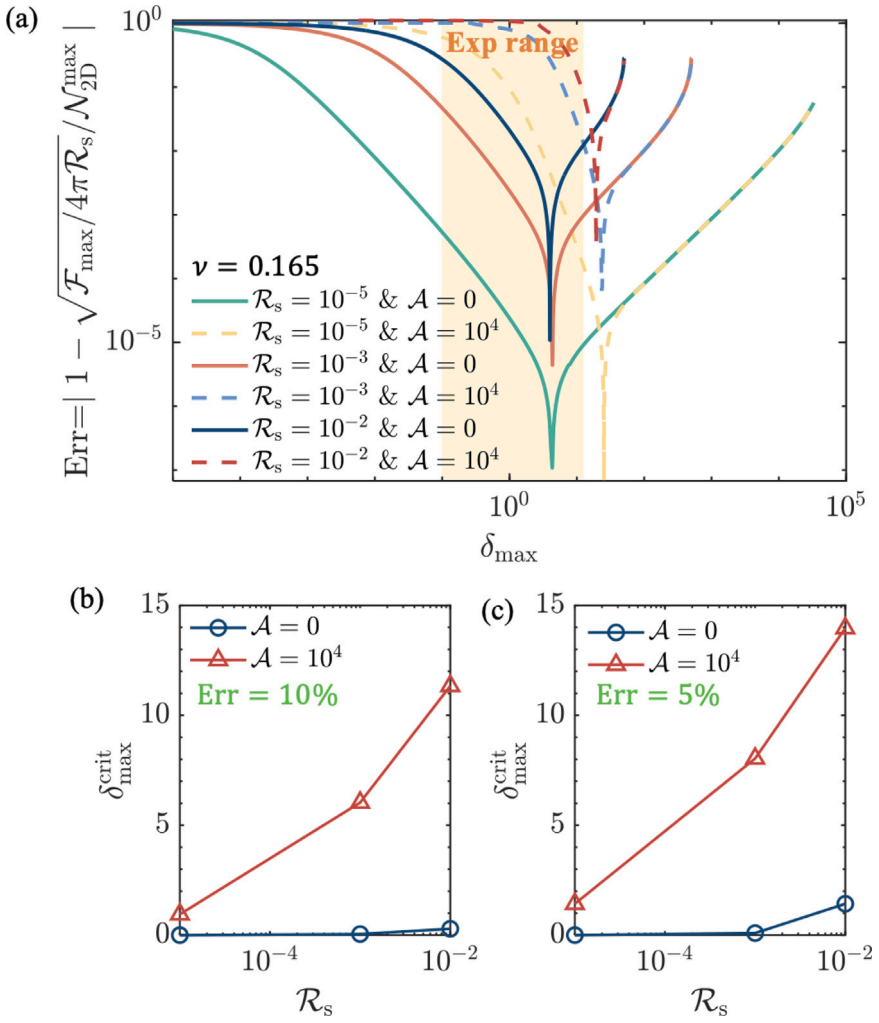


Fig. 5. (a) The error (Err) induced by using Eq. (2) to determine the breaking strength of the material, rather than relying on numerical solutions. The orange zone indicates experimentally accessible ranges of δ. The lower thresholds of the desired indentation depth before rupture ($\delta_{\max}^{\mathrm{crit}}$) to ensure the error remains within (b) 10% and (c) 5%, respectively.

at $\mathcal{T} \to 0$. Specifically, the case with finite shear resistance (i.e., $\mathcal{T} = 10$) collapses to the frictionless limit at large deflections within the experimental range (refer to Table 3 for details). To understand this behavioral transition, we further investigate the size of the shear zone in the peripheral region of the membrane/supporting substrate contacts.

Figure 11a shows the evolution of the dimensionless size of the shear zone (ρ_o) with $\mathcal{F}^{2/3}/\mathcal{T}$ with varying $\mathcal{T}$ when $\mathcal{R}_s = 10^{-3}$. The asymptotic solution for ρ_o, modified from Dai and Lu (2021)'s work, is written as,

$$\rho_o \sim [1 + \frac{6\mathcal{F}^{2/3}}{(1-\nu)(2\pi^2)^{2/3}\mathcal{T}}]^{1/3}. \tag{32}$$

This expression aligns with the numerical solutions at $\mathcal{T} > 1$, which is the range of shear resistances observed in the experiments (see Table 3 for details). Figure 11b compares the numerical results with this asymptote to vary $\mathcal{R}_s$ when $\mathcal{T} = 10$, showing good agreement and further validating the precision of this expression.

To extract the 2D Young's modulus (E_{2D}) from load–deflection measurements, it is crucial to establish a load–deflection relationship that considers both the sliding effect ($\mathcal{T}$) and the tip size ($\mathcal{R}_s$). We begin with a scaling analysis: the work done by the indentation force is $W \sim Fd$, and the energy dissipated by the interfacial slippage is $U \sim \tau_{ms}\epsilon a^3(\rho_o - 1)$, with the typical strain ϵ being d^2/a^2. Balancing these terms leads to $\mathcal{F} \sim \mathcal{T}\delta(\rho_o - 1)$, capturing the behaviors transitioning from small to large indentations.

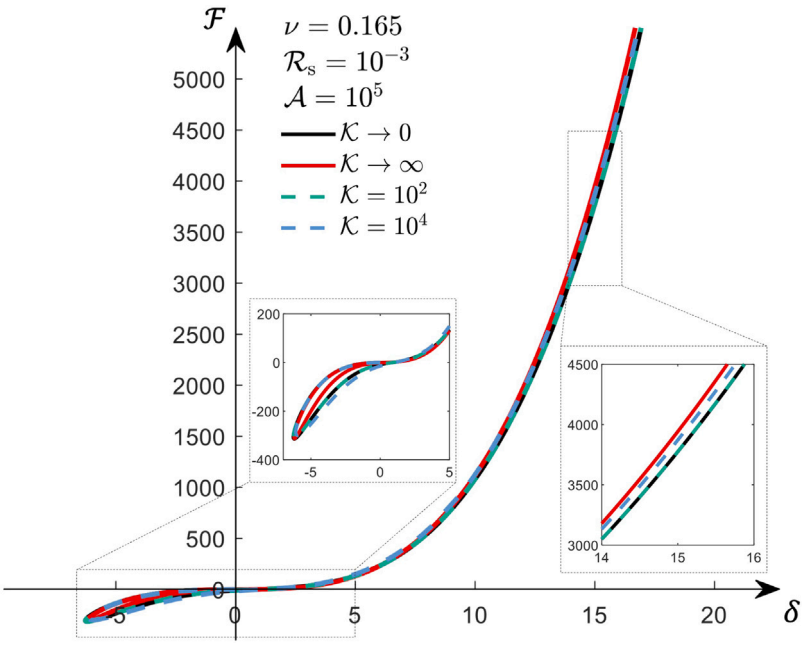


Fig. 6. $\mathcal{F}$ vs. δ for various friction numbers $\mathcal{K}$ when $\mathcal{R}_s = 10^{-3}$ and $\mathcal{A} = 10^5$ are fixed.

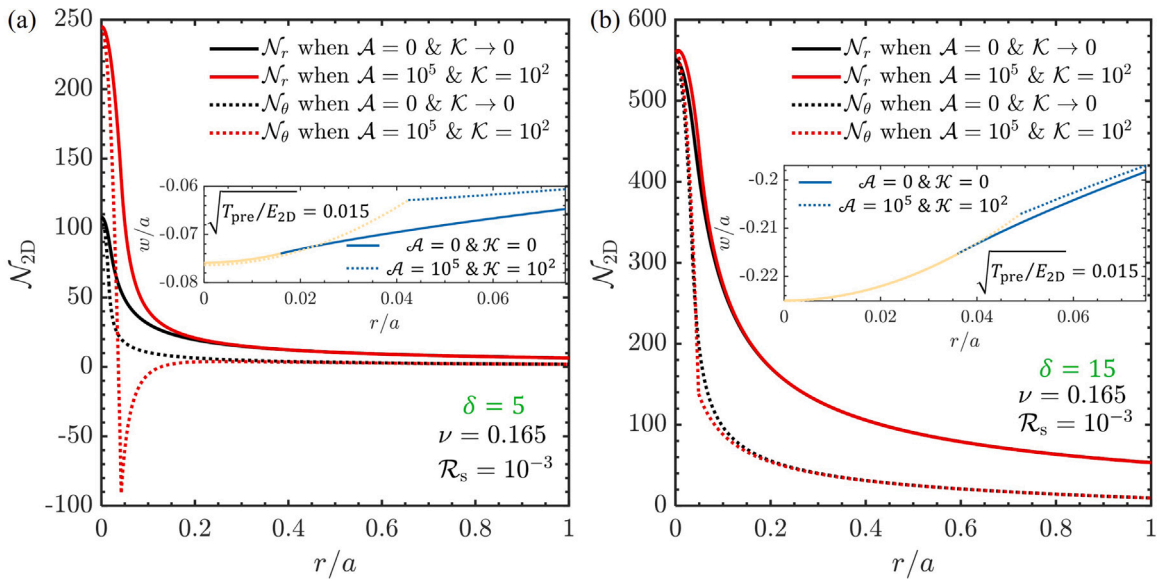


Fig. 7. The dimensionless radial and hoop membrane stress distributions at (a) $\delta = 5$ and (b) $\delta = 15$, respectively. Inset: The corresponding normalized profiles of the indented membrane near the spherical tip. The yellow and blue colors indicate the contact and noncontact regions, respectively.

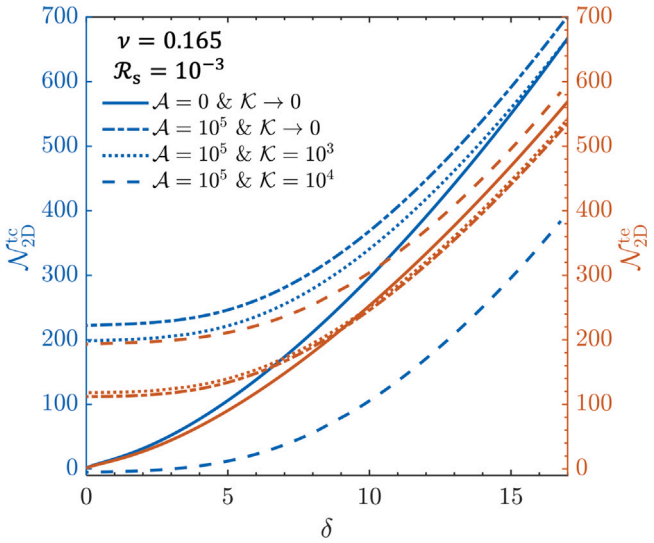


Fig. 8. The dimensionless membrane stress at the center, $\mathcal{N}_{2D}^{tc}$, vs. δ (blue), and the dimensionless membrane stress at the tip-membrane contact line, $\mathcal{N}_{2D}^{ec}$, vs. δ (red).

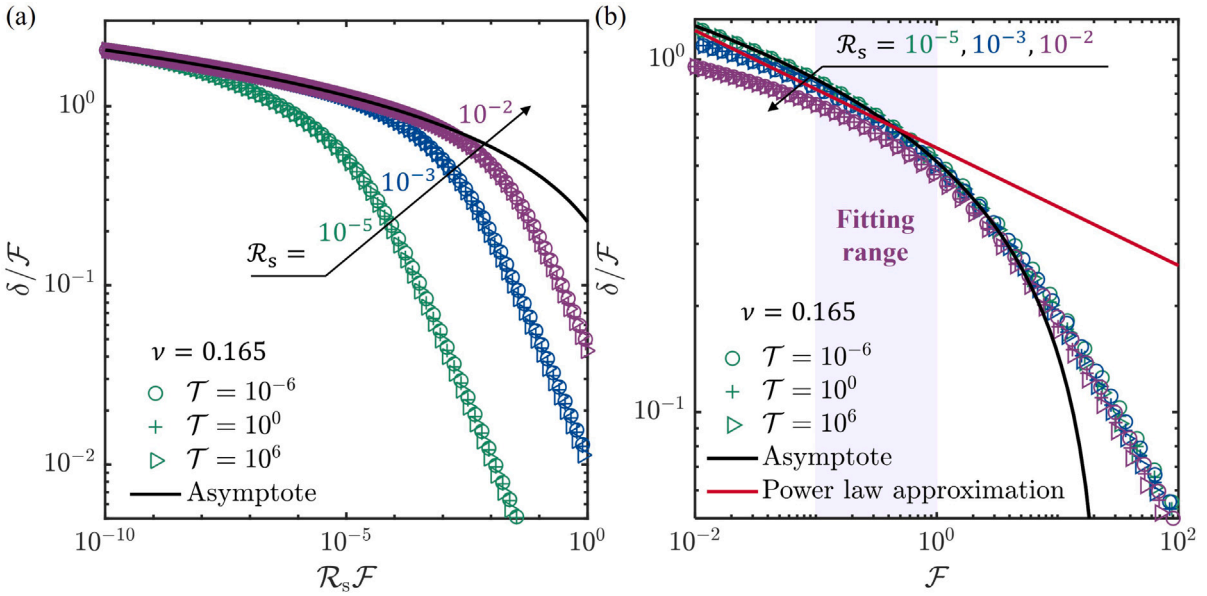


Fig. 9. (a) $\delta/\mathcal{F}$ vs. $\mathcal{R}_s\mathcal{F}$ for various $\mathcal{R}_s$ and shear numbers $\mathcal{T}$. The asymptotic solutions are given by Eq. (29) when $\mathcal{F} \ll \mathcal{R}_s \ll 1$. (b) $\delta/\mathcal{F}$ vs. $\mathcal{F}$ for various $\mathcal{R}_s$ and shear numbers $\mathcal{T}$. The asymptotic solutions are given by Eq. (29) when $\mathcal{R}_s \ll \mathcal{F} \ll 1$. The approximate solutions, given by Eq. (30), are obtained through power law fitting of the numerical data (indicated by markers) within the fitting range indicated by the purple background.

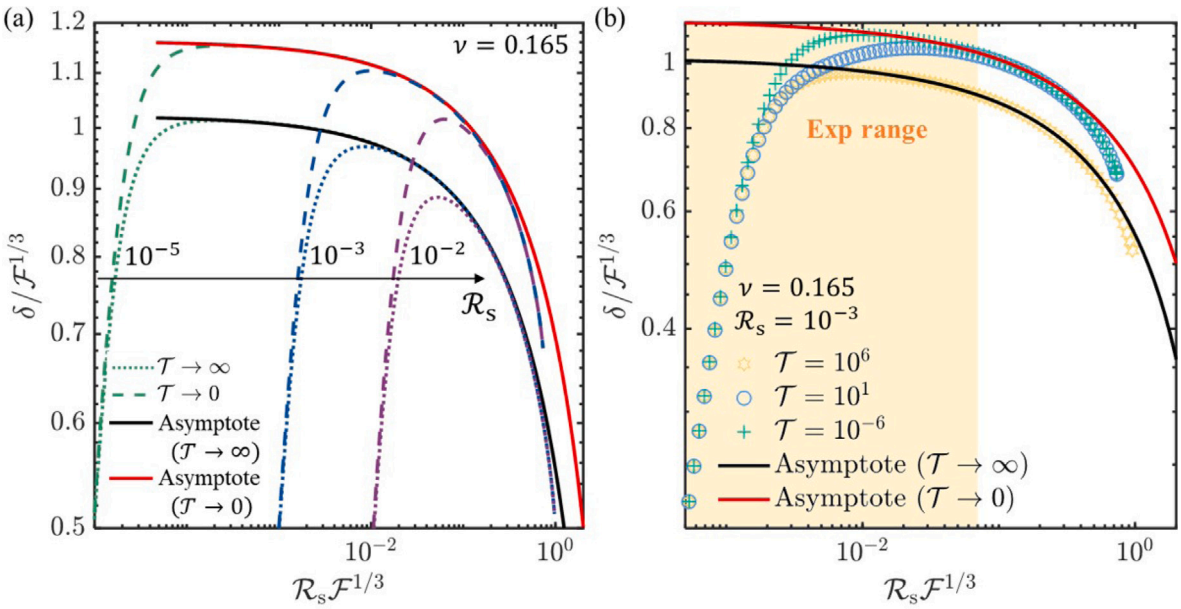


Fig. 10. (a) $\delta/\mathcal{F}^{1/3}$ vs. $\mathcal{R}_s\mathcal{F}^{1/3}$ for various $\mathcal{R}_s$ at the two limits: the fixed edge ($\mathcal{T} \to \infty$) (black) and the frictionless edge ($\mathcal{T} \to 0$) (red). (b) $\delta/\mathcal{F}^{1/3}$ vs. $\mathcal{R}_s\mathcal{F}^{1/3}$ for various $\mathcal{T}$ when $\mathcal{R}_s = 10^{-3}$. Here, the asymptotic solutions to the two limiting cases are given by Eq. (31).

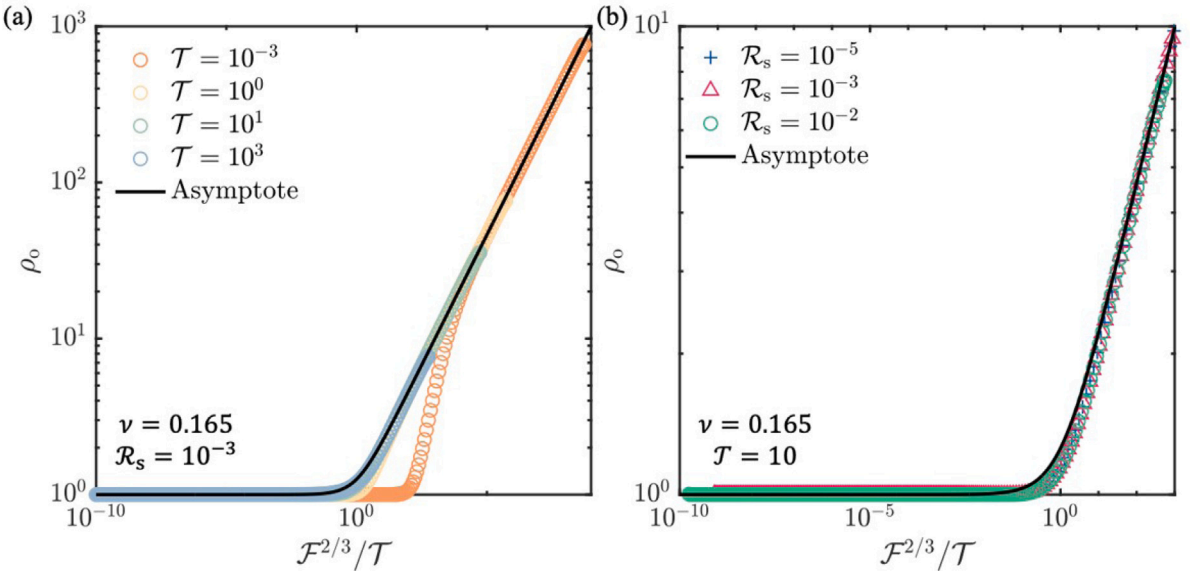


Fig. 11. The dimensionless size of the shear zone, ρ_o, vs. $\mathcal{F}^{2/3}/\mathcal{T}$ for (a) various $\mathcal{T}$ when $\mathcal{R}_s = 10^{-3}$, and (b) various $\mathcal{R}_s$ when $\mathcal{T} = 10$. The asymptotic solutions are given by Eq. (32).

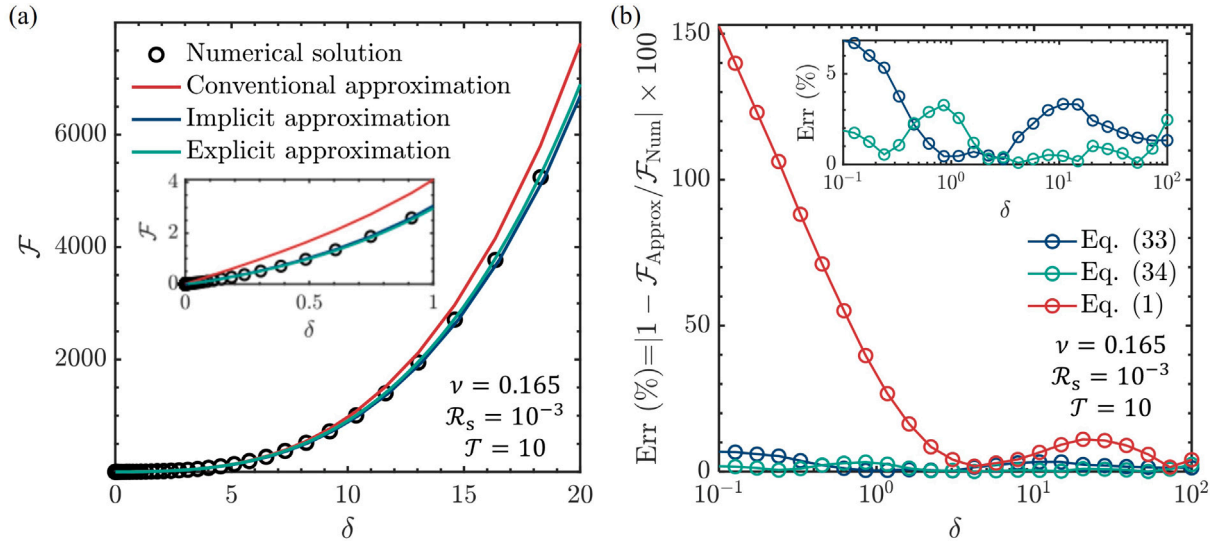


Fig. 12. (a) $\mathcal{F}$ vs. δ obtained from numerical solutions, Eq. (1) (Schwerin-type approximation), Eq. (33) (our implicit approximation), and Eq. (34) (our explicit approximation) when $\mathcal{R}_s = 10^{-3}$ and $\mathcal{T} = 10$. (b) Comparison of the errors of the three approximations relative to the numerical solutions.

By combining the small (Eq. (30)), intermediate, and large (Eq. (31)) indentation regimes through a superposition method, we derive the following new approximation of the F-d relationship which accounts for the effects of interfacial sliding and tip size

$$\mathcal{F} \approx 2\delta^{1.2} + \frac{(1-\nu)(2\pi^2)^{\frac{2}{3}}}{2}\mathcal{T}\frac{\delta^3}{\mathcal{F}^{\frac{2}{3}}}\left(\rho_o - 1\right)\left[\frac{1}{\left[1.05-0.15\nu-0.16\nu^2-\frac{2\left(\sqrt{2}-1\right)}{\sqrt{\pi}}\sqrt{\mathcal{R}_s\mathcal{F}^{\frac{1}{3}}}\right]^3} - \frac{1}{\left[\left(\frac{\pi}{2}\right)^{\frac{1}{3}}-\frac{2\left(\sqrt{2}-1\right)}{\sqrt{\pi}}\sqrt{\mathcal{R}_s\mathcal{F}^{\frac{1}{3}}}\right]^3}\right], \quad (33)$$
$$+\frac{\delta^3}{\left[\left(\frac{\pi}{2}\right)^{\frac{1}{3}}-\frac{2\left(\sqrt{2}-1\right)}{\sqrt{\pi}}\sqrt{\mathcal{R}_s\mathcal{F}^{\frac{1}{3}}}\right]^3}$$

where ρ_o is given by Eq. (32). The coefficients in the second and third terms on the right-hand side are determined by the following criteria: when $\mathcal{T} \to \infty$, Eq. (33) reduces to $\mathcal{F} \approx 2\delta^{1.2} + \delta^3/[1.05 - 0.15\nu - 0.16\nu^2 - \frac{2(\sqrt{2}-1)}{\sqrt{\pi}}\sqrt{\mathcal{R}_s\mathcal{F}^{1/3}}]^3$, representing the limiting case of a fixed edge; when $\mathcal{T} \to 0$, Eq. (33) reduces to $\mathcal{F} \approx 2\delta^{1.2} + \delta^3/[(\frac{\pi}{2})^{1/3} - \frac{2(\sqrt{2}-1)}{\sqrt{\pi}}\sqrt{\mathcal{R}_s\mathcal{F}^{1/3}}]^3$, representing the limiting case of a frictionless edge.

Furthermore, we propose an explicit formula to address the difficulties encountered with the implicit formula given by Eq. (33) during the fitting procedure. This explicit formula is derived by substituting $\mathcal{F} \sim 2\delta^3/\pi$ into the right-hand side of Eq. (33), and is written as

$$\mathcal{F} \approx 2\delta^{1.2} + \frac{(1-\nu)\pi^2}{2}\mathcal{T}\delta\left(\rho_o - 1\right)\left[\frac{1}{\left[1.05-0.15\nu-0.16\nu^2-\frac{2\left(\sqrt{2}-1\right)}{\sqrt{\pi}}\sqrt{\mathcal{R}_s\left(\frac{2}{\pi}\right)^{1/3}\delta}\right]^3} - \frac{1}{\left[\left(\frac{\pi}{2}\right)^{\frac{1}{3}}-\frac{2\left(\sqrt{2}-1\right)}{\sqrt{\pi}}\sqrt{\mathcal{R}_s\left(\frac{2}{\pi}\right)^{1/3}\delta}\right]^3}\right], \quad (34)$$
$$+\frac{\delta^3}{\left[\left(\frac{\pi}{2}\right)^{\frac{1}{3}}-\frac{2\left(\sqrt{2}-1\right)}{\sqrt{\pi}}\sqrt{\mathcal{R}_s\left(\frac{2}{\pi}\right)^{1/3}\delta}\right]^3}$$

where $\rho_o \sim [1 + \frac{6\delta^2}{(1-\nu)\pi^2\mathcal{T}}]^{1/3}$.

Figure 12a compares the numerical solutions with the conventional approximation given by Eq. (1), as well as the implicit and explicit approximations given by Eqs. (33)–(34), respectively. As illustrated, the proposed solution demonstrates much better agreement with numerical solutions than the conventional approximation within the experimental range when $\mathcal{R}_s = 10^{-3}$ and $\mathcal{T} = 10$. Figure 12b presents the relative error percentage (denoted as Err(%) $= |1 - \mathcal{F}_{Approx}/\mathcal{F}_{Num}| \times 100$) for both implicit and

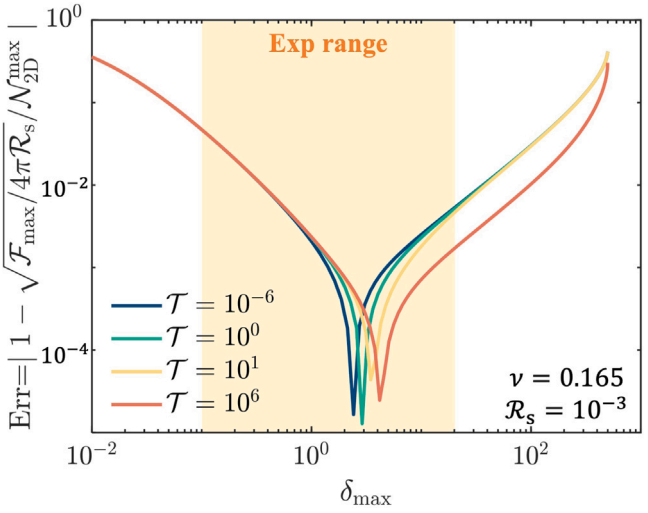


Fig. 13. The error (Err) in the maximum membrane stress induced by Eq. (2) relative to the numerical solutions for varying $\mathcal{T}$ when $\mathcal{R}_s = 10^{-3}$ is fixed.

explicit approximations compared to numerical results. As shown, the error for both approximations remains within 10% regardless of the indentation depth when $\mathcal{R}_s = 10^{-3}$ and $\mathcal{T} = 10$, which are parameters commonly observed in experiments (see Table 3 for details). Therefore, Eq. (34) shows promise for simultaneously extracting the in-plane stiffness of the membrane and the shear strength at the membrane-substrate interface from load–deflection measurements, achieving higher accuracy compared to the widely used formulation Eq. (1).

Figure 13 demonstrates the negligible influence of sliding contacts between the membrane and the substrate on the maximum 2D membrane stress when $\mathcal{R}_s = 10^{-3}$, with varying $\mathcal{T}$. This observation suggests that Eq. (2) remains applicable for extracting the breaking strength from the measurements of the fracture force, even when considering sliding contacts with different shear resistances.

5.4. Applicability of our model

When employing the proposed formulation in Eq. (34) to simultaneously evaluate E_{2D} and τ_{ms} based on load–deflection measurements in indentation tests, several factors can affect the applicability of our model. The first factor is the bending stiffness of the suspended film as its thickness increases. To address this, we perform a scaling analysis comparing the stretching and bending energies during drumhead nanoindentation. With typical film strain $\epsilon \sim d^2/a^2$ and curvature $\kappa \sim d/a^2$, we estimate the pre-stretching energy as $U_{pre} \sim T_{pre}\epsilon a^2 \sim T_{pre}d^2$, the stretching energy as $U_s \sim E_{2D}\epsilon^2 a^2 \sim E_{2D}d^4/a^2$, and the bending energy as $U_b \sim B\kappa^2 a^2 \sim Bd^2/a^2$, where B is the bending stiffness. The ratio $U_{pre}/U_s \sim T_{pre}a^2/E_{2D}d^2$ indicates that prestress dominates within small deflections (i.e., $d \ll L = \sqrt{T_{pre}/E_{2D}}a$), while membrane stretching dominates within large deflections (i.e., $d \gg L$) if bending stiffness is negligible, validating the above numerical analysis. For small deflections, comparing the bending energy to the pre-stretching energy, $U_b/U_{pre} \sim B/T_{pre}a^2$, gives a dimensionless parameter $\mathcal{B}_\alpha = B/T_{pre}a^2$ to access bending effects. For large deflections, comparing the bending energy to the stretching energy, $U_b/U_s \sim B/E_{2D}d^2$, gives another parameter $\mathcal{B}_\beta = B/E_{2D}d^2$. Bending stiffness can be considered negligible if $\mathcal{B}_\alpha \ll 1$ for small deflections and $\mathcal{B}_\beta \ll 1$ for large deflections, as satisfied by nanoindentation experiments on monolayer 2D materials listed in Table 1. Otherwise, bending dominates, leading to $Fd \sim U_b$, with $F \sim Bd/a^2$, suggesting a linear relationship between the indentation force and depth. It should be noted that for multilayer 2D materials, including heterogeneous 2D materials, the actual bending stiffness tends to be lower than predicted by Euler–Bernoulli beam theory due to interlayer shear (Huang et al., 2023; Wang et al., 2024b).

Another factor is associated with the challenge of determining the starting point (the zero displacement point) of the load–deflection curve $F(d)$, where the indentation force F is defined as zero when $d = 0$ (see Fig. 1c). In reality, the force F applied to the membrane is non-zero when $d = 0$ if there are tip-membrane interactions as discussed in this paper. This discrepancy arises because the suspended membrane is already subjected to some load when it appears to be flat (i.e., $d = 0$) in the measurement. This issue has been shown to significantly affect the accuracy of the estimation of the Young's modulus of 2D materials E_{2D} using Eq. (1) (Lin et al., 2013).

Our proposed formulation, Eq. (34), introduces an additional unknown parameter, τ_{ms}, into the fitting process. This inclusion potentially exacerbates the impact of inaccuracies in determining the zero displacement point on the extraction of mechanical and interfacial properties. Moreover, the precision of the estimated properties might decrease since Eq. (34) requires fitting three unknowns (i.e., T_{pre}, E_{2D}, and τ_{ms}) instead of two (i.e., T_{pre} and E_{2D}) as in Eq. (1). To overcome this challenge, it is essential to explore advanced data-driven and model-driven methods, such as solution-guided machine learning (Wang et al., 2024a). These methods

offer promising avenues for improving the efficiency and accuracy of extraction of properties from drumhead nanoindentation. Given these considerations, in a follow-up research, we intend to focus on extensive experimental data analysis rather than attempt to resolve all the limitations of the current theoretical framework.

6. Concluding remarks

In this study, we have explored the effects of tip-membrane and membrane-substrate interfacial interactions on the nanoindentation of drumhead specimens, focusing on 2D materials suspended over a circular microhole. Our boundary value problem incorporates key factors such as prestress, membrane elasticity, finite tip size, adhesion, and friction at the tip-membrane interface, as well as the slippage at the membrane-substrate interface.

The primary findings of this investigation are summarized as follows:

- *Tip-Membrane Interactions*: The adhesion and friction at the tip-membrane interface slightly influence the load–deflection relationship during indentation, while significantly modifying the membrane stress distribution, particularly under moderate deflections (i.e., $\delta \sim \mathcal{O}(1)$). Our analysis shows that the adhesive effects decrease with increasing indentation depth or decreasing tip size. Furthermore, as the indentation depth and the interfacial shear stress increase, the frictional interaction shifts the maximum membrane stress from the center to the contact line between the tip and the membrane. To mitigate undesired adhesive and frictional effects when extracting in-plane Young's modulus and breaking strength from load–deflection measurements, smaller tip sizes (e.g., $\mathcal{R}_s \lesssim 10^{-3}$) should be selected, and measurement data with $\delta \leq 1$ should be excluded from data analysis if using the widely used Schwerin-type formulations (Eqs. (1)–(2)).
- *Membrane-Substrate Slippage*: The slippage of the membrane against its supporting substrate induces a transition under large deformation from one limiting case, characterized by a fixed edge, to another limiting case, characterized by a frictionless edge. Furthermore, our findings suggest that within the experimental ranges of tip radius and shear resistance, membrane-substrate slippage have a negligible impact on the maximum 2D membrane stress. This indicates that the simplified expression, Eq. (2), remains effective in accurately predicting the breaking strength from fracture force measurements if the adhesion and friction at the tip-membrane interface are both negligible. Additionally, to facilitate more accurate extraction of the mechanical properties out of drumhead indentation tests, we have proposed an approximate solution, Eq. (34), for the load–deflection relation. This solution accounts for membrane-substrate interfacial slippage and the finite tip size, providing a means to simultaneously and accurately extract crucial material and interfacial properties, such as modulus and shear strength, by fitting the proposed models to experimentally measured data.

In summary, this study provides a more comprehensive understanding of the mechanical behaviors of ultrathin membranes under nanoindentation, with implications for the metrology and design of such membranes in various applications.

CRediT authorship contribution statement

Yifan Rao: Writing – original draft, Writing – review & editing, Visualization, Validation, Software, Methodology, Investigation, Formal analysis, Data curation, Conceptualization. **Nanshu Lu:** Writing – review & editing, Supervision, Resources, Project administration, Methodology, Conceptualization.

Declaration of competing interest

The authors declare that they have no known competing financial interests or personal relationships that could have appeared to influence the work reported in this paper.

Data availability

Data will be made available on request.

Acknowledgments

We extend our heartfelt wishes to Prof. Gao for a very happy and prosperous 60^{th} birthday, celebrating his seminal contributions to the scientific community and his profound impact on our work.

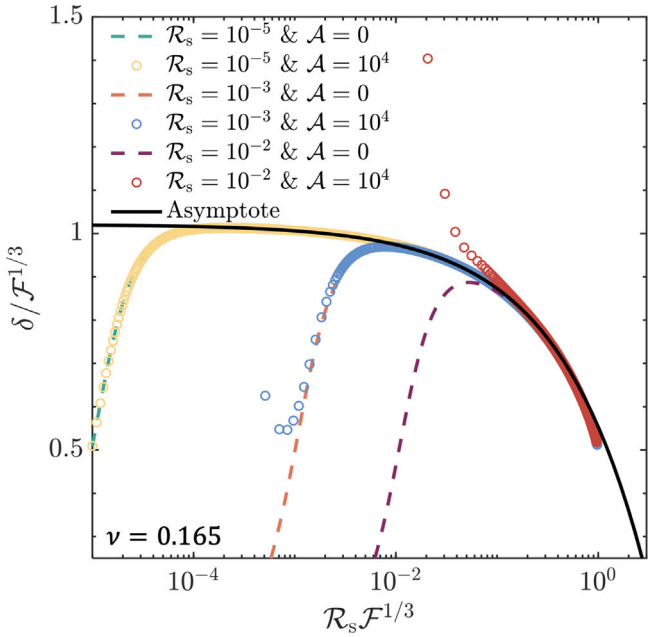


Fig. B.1. $\delta/\mathcal{F}^{1/3}$ vs. $\mathcal{R}_s\mathcal{F}^{1/3}$ under various $\mathcal{R}_s$ and $\mathcal{A}$. The asymptotic solutions are given by Eq. (31) at $\mathcal{T} \to \infty$ (i.e., the asymptote for drumhead nanoindentation with a fixed edge using a non-adhesive and frictionless spherical tip of finite radius).

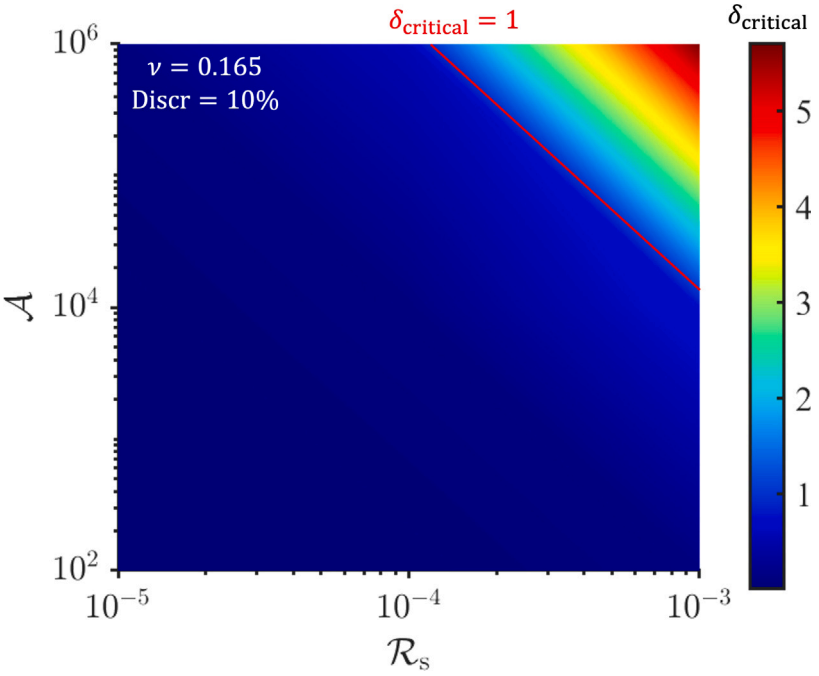


Fig. B.2. Contour curves for the critically dimensionless indentation depth (δ_{critical}) with Discr = 10% in $\mathcal{A} \sim \mathcal{R}_s$ parametric space for drumhead nanoindentation under an adhesive and frictionless spherical tip of finite radius.

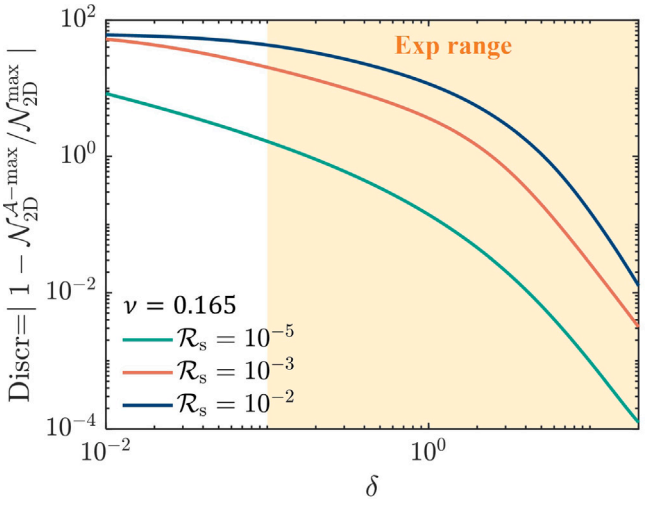


Fig. B.3. The discrepancy of the maximum 2D membrane stresses (Discr) between the adhesive tip case (i.e., $\mathcal{N}_{2D}^{\mathcal{A}-\max}$ when $\mathcal{A} = 10^4$) and the non-adhesive tip case (i.e., $\mathcal{N}_{2D}^{\max}$ when $\mathcal{A} = 0$) at the same indentation depth.

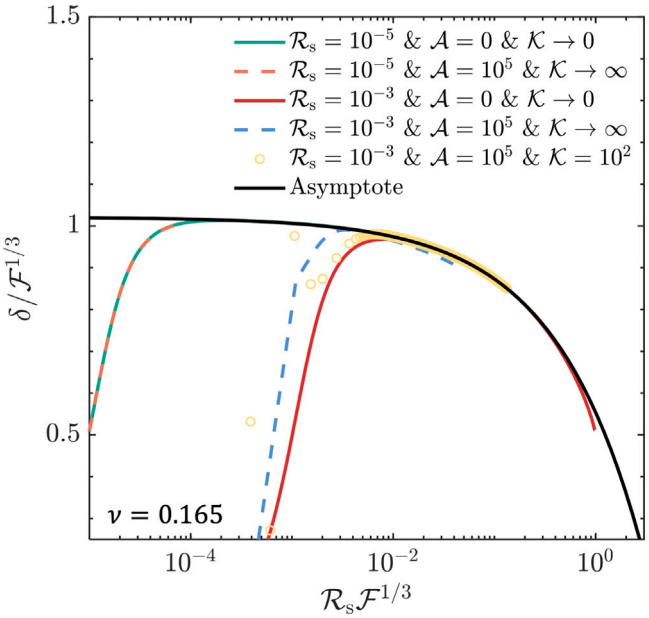


Fig. B.4. $\delta/\mathcal{F}^{1/3}$ vs. $\mathcal{R}_s\mathcal{F}^{1/3}$ under various $\mathcal{R}_s$ when considering a fixed edge and two types of tip/membrane contacts: the non-adhesive and frictionless contact ($\mathcal{A} = 0$ & $\mathcal{K} \to 0$) and the adhesive and non-slip contact ($\mathcal{A} = 10^5$ & $\mathcal{K} \to \infty$). The asymptotic solutions are given by Eq. (31) at $\mathcal{T} \to \infty$ (i.e., the asymptote for drumhead nanoindentation with a fixed edge using a non-adhesive and frictionless spherical tip of finite radius).

Appendix A. Derivation of boundary conditions at $a = a_{in}$

The total free energy of a suspended membrane indented by an adhesive and frictional spherical tip can be expressed as a functional of the form

$$\Pi = \int_0^{a_{in}} \pounds_\alpha dr + \int_{a_{in}}^{a} \pounds_\beta dr + \int_a^{a_{out}} \pounds_\gamma dr, \tag{A.1}$$

where

$$\begin{cases} \pounds_\alpha = 2\pi r[\phi_\alpha - \Gamma_{tm} - p(r)w(r) + \tau_{tm}(u(r) - u_{ref}^{in}(r))] \\ \pounds_\beta = 2\pi r\phi_\beta \\ \pounds_\gamma = 2\pi r[\phi_\gamma - \tau_{ms}(u(r) - \frac{(1-\nu)T_{pre}}{E_{2D}}r)] \end{cases}. \tag{A.2}$$

Here, $\phi_i (i = \alpha, \beta, \gamma)$ is the stretching energy density of the indented membrane, defined as $\phi_i = \frac{E_{2D}}{2(1-\nu^2)}[(u' + \frac{w'^2}{2})^2 + \frac{u^2}{r^2} + 2\nu(u' + \frac{w'^2}{2})\frac{u}{r}]$, $p(r)$ represents the contact pressure between the tip and the membrane, and $u_{\mathrm{ref}}^{\mathrm{in}}(r)$ represents the distribution of the radial displacement at $r \in [0, a_{\mathrm{in}}]$ for a reference state where the membrane fully sticks to the tip during indentation. We assume $u_{\mathrm{ref}}^{\mathrm{in}}(r) = \frac{(1-\nu)T_{\mathrm{pre}}}{E_{2D}} r$ in this work.

At equilibrium, the variation $\delta\Pi$ must be zero with respect to arbitrary but kinematically admissible variables δa_{in}, δa_{out}, δu, and δw, which leads to

$$\delta\Pi = \int_0^{a_{\mathrm{in}}} \delta\mathcal{L}_\alpha dr + \int_{a_{\mathrm{in}}}^{a} \delta\mathcal{L}_\beta dr + \int_a^{a_{\mathrm{out}}} \delta\mathcal{L}_\gamma dr + \mathcal{L}_\alpha \delta a_{\mathrm{in}} - \mathcal{L}_\beta \delta a_{\mathrm{in}} + \mathcal{L}_\gamma \delta a_{\mathrm{out}} = 0. \tag{A.3}$$

Since w is prescribed in the contact (i.e., $r \in [0, a_{\mathrm{in}}]$) and the supported (i.e., $r \in [a, a_{\mathrm{out}}]$) regions, $\delta w = 0$. Applying the fundamental lemma of calculus of variations, we obtain the Euler–Lagrange equation

$$\frac{\partial \mathcal{L}_i}{\partial u} - \frac{\mathrm{d}}{\mathrm{d}r}\left(\frac{\partial \mathcal{L}_i}{\partial u'}\right) = 0, \tag{A.4}$$

for $i = \alpha, \gamma$. Substituting Eqs. (A.1) and (A.2) in Eq. (A.4), we derive the in-plane equilibrium Eqs. (7) and (8), which are the in-plane equilibrium equations for these two regions.

Additionally, for frictional contacts between the spherical tip and the membrane (i.e., the value of τ_{tm} is finite), varying a_{in} results in a variation of Π that satisfies

$$\delta\Pi_{a_{\mathrm{in}}} = [\mathcal{L}_\alpha(a_{\mathrm{in}}^-) - \mathcal{L}_\beta(a_{\mathrm{in}}^+) - \frac{\partial \mathcal{L}_\beta(a_{\mathrm{in}}^+)}{\partial w'}(w'(a_{\mathrm{in}}^-) - w'(a_{\mathrm{in}}^+))]\delta a_{\mathrm{in}} = 0. \tag{A.5}$$

Similarly, infinitesimal variations in $u(a_{\mathrm{in}})$ yield

$$\delta\Pi_u = [\frac{\partial \mathcal{L}_\alpha(a_{\mathrm{in}}^-)}{\partial u'} - \frac{\partial \mathcal{L}_\beta(a_{\mathrm{in}}^+)}{\partial u'}]\delta u(a_{\mathrm{in}}) = 0. \tag{A.6}$$

Boundary conditions Eqs. (16)–(18) are derived to satisfy them as $\delta a_{\mathrm{in}} \neq 0$ and $\delta u(a_{\mathrm{in}}) \neq 0$.

For a non-slip tip ($\tau_{\mathrm{tm}} \to \infty$), $u(r) = u_{\mathrm{ref}}^{\mathrm{in}}(r)$ in Eq. (A.2). Meanwhile, $\delta u(a_{\mathrm{in}}) = 0$ leads to a discontinuity in radial membrane stress at $a = a_{\mathrm{in}}$. In this case, varying a_{in} results in a variation of Π that satisfies

$$\delta\Pi_{a_{\mathrm{in}}} = [\mathcal{L}_\alpha(a_{\mathrm{in}}^-) - \mathcal{L}_\beta(a_{\mathrm{in}}^+) - \frac{\partial \mathcal{L}_\beta(a_{\mathrm{in}}^+)}{\partial w'}(w'(a_{\mathrm{in}}^-) - w'(a_{\mathrm{in}}^+)) - \frac{\partial \mathcal{L}_\beta(a_{\mathrm{in}}^+)}{\partial u'}(u'(a_{\mathrm{in}}^-) - u'(a_{\mathrm{in}}^+))]\delta a_{\mathrm{in}} = 0, \tag{A.7}$$

which leads to the first equation of Eq. (19) as $\delta a_{\mathrm{in}} \neq 0$. Detailed derivations of these equations can be found in Refs. Majidi and Adams (2009) and Rao et al. (2021, 2023).

Appendix B. Supplementary figures

See Figs. B.1–B.4.

References

Akinwande, D., Brennan, C.J., Bunch, J.S., Egberts, P., Felts, J.R., Gao, H., Huang, R., Kim, J.-S., Li, T., Li, Y., et al., 2017. A review on mechanics and mechanical properties of 2D materials—Graphene and beyond. Extreme Mech. Lett. 13, 42–77.

Al-Quraishi, K.K., He, Q., Kauppila, W., Wang, M., Yang, Y., 2020. Mechanical testing of two-dimensional materials: a brief review. Int. J. Smart Nano Mater. 11 (3), 207–246.

Begley, M.R., Mackin, T.J., 2004. Spherical indentation of freestanding circular thin films in the membrane regime. J. Mech. Phys. Solids 52 (9), 2005–2023.

Bertolazzi, S., Brivio, J., Kis, A., 2011. Stretching and breaking of ultrathin MoS2. ACS Nano 5 (12), 9703–9709.

Bhatia, N.M., Nachbar, W., 1968. Finite indentation of an elastic membrane by a spherical indenter. Int. J. Non-Linear Mech. 3 (3), 307–324.

Borodich, F.M., Galanov, B.A., Suarez-Alvarez, M.M., 2014. The JKR-type adhesive contact problems for power-law shaped axisymmetric punches. J. Mech. Phys. Solids 68, 14–32.

Cao, G., Gao, H., 2019. Mechanical properties characterization of two-dimensional materials via nanoindentation experiments. Prog. Mater. Sci. 103, 558–595.

Cao, Z., Wang, P., Gao, W., Tao, L., Suk, J., Ruoff, R., Akinwande, D., Huang, R., Liechti, K., 2014. A blister test for interfacial adhesion of large-scale transferred graphene. Carbon 69, 390–400.

Cartamil-Bueno, S.J., Cavalieri, M., Wang, R., Houri, S., Hofmann, S., van der Zant, H.S., 2017. Mechanical characterization and cleaning of CVD single-layer h-BN resonators. NPJ 2D Mater. Appl. 1 (1), 16.

Castellanos-Gomez, A., Poot, M., Steele, G.A., Van Der Zant, H.S., Agraït, N., Rubio-Bollinger, G., 2012a. Elastic properties of freely suspended MoS2 nanosheets. Adv. Mater. 24 (6), 772–775.

Castellanos-Gomez, A., Poot, M., Steele, G.A., Van der Zant, H.S., Agraït, N., Rubio-Bollinger, G., 2012b. Mechanical properties of freely suspended semiconducting graphene-like layers based on MoS 2. Nanoscale Res. Lett. 7, 1–4.

Chandler, T.G., Vella, D., 2020. Indentation of suspended two-dimensional solids: The signatures of geometrical and material nonlinearity. J. Mech. Phys. Solids 144, 104109.

Cooper, R.C., Lee, C., Marianetti, C.A., Wei, X., Hone, J., Kysar, J.W., 2013. Nonlinear elastic behavior of two-dimensional molybdenum disulfide. Phys. Rev. B 87 (3), 035423.

Dai, Z., Hou, Y., Sanchez, D.A., Wang, G., Brennan, C.J., Zhang, Z., Liu, L., Lu, N., 2018. Interface-governed deformation of nanobubbles and nanotents formed by two-dimensional materials. Phys. Rev. Lett. 121 (26), 266101.

Dai, Z., Liu, L., Zhang, Z., 2019. Strain engineering of 2D materials: issues and opportunities at the interface. Adv. Mater. 31 (45), 1805417.

Dai, Z., Lu, N., 2021. Poking and bulging of suspended thin sheets: Slippage, instabilities, and metrology. J. Mech. Phys. Solids 149, 104320.

Dai, Z., Lu, N., Liechti, K.M., Huang, R., 2020. Mechanics at the interfaces of 2D materials: Challenges and opportunities. Curr. Opin. Solid State Mater. Sci. 24 (4), 100837.
Dai, Z., Rao, Y., Lu, N., 2022. Two-dimensional crystals on adhesive substrates subjected to uniform transverse pressure. Int. J. Solids Struct. 257, 111829.
Deng, Z., Klimov, N.N., Solares, S.D., Li, T., Xu, H., Cannara, R.J., 2013. Nanoscale interfacial friction and adhesion on supported versus suspended monolayer and multilayer graphene. Langmuir 29 (1), 235–243.
Di Giorgio, C., Blundo, E., Pettinari, G., Felici, M., Bobba, F., Polimeni, A., 2022. Mechanical, elastic, and adhesive properties of two-dimensional materials: From straining techniques to state-of-the-art local probe measurements. Adv. Mater. Interfaces 9 (13), 2102220.
Dong, Y., Wu, X., Martini, A., 2013. Atomic roughness enhanced friction on hydrogenated graphene. Nanotechnology 24 (37), 375701.
Falin, A., Cai, Q., Santos, E.J., Scullion, D., Qian, D., Zhang, R., Yang, Z., Huang, S., Watanabe, K., Taniguchi, T., et al., 2017. Mechanical properties of atomically thin boron nitride and the role of interlayer interactions. Nature Commun. 8 (1), 15815.
Han, Y., Gao, L., Zhou, J., Hou, Y., Jia, Y., Cao, K., Duan, K., Lu, Y., 2022. Deep elastic strain engineering of 2D materials and their twisted bilayers. ACS Appl. Mater. Interfaces 14 (7), 8655–8663.
Han, Y., Zhou, J., Wang, H., Gao, L., Feng, S., Cao, K., Xu, Z., Lu, Y., 2021. Experimental nanomechanics of 2D materials for strain engineering. Appl. Nanosci. 11, 1075–1091.
Huang, Z., He, Z., Zhu, Y., Wu, H., 2023. A general theory for the bending of multilayer van der Waals materials. J. Mech. Phys. Solids 171, 105144.
Jang, H., Sel, K., Kim, E., Kim, S., Yang, X., Kang, S., Ha, K.-H., Wang, R., Rao, Y., Jafari, R., et al., 2022. Graphene e-tattoos for unobstructive ambulatory electrodermal activity sensing on the palm enabled by heterogeneous serpentine ribbons. Nature Commun. 13 (1), 1–13.
Jiang, J.-W., Park, H.S., 2015. A Gaussian treatment for the friction issue of lennard-jones potential in layered materials: Application to friction between graphene, MoS2, and black phosphorus. J. Appl. Phys. 117 (12).
Jiang, T., Zhu, Y., 2015. Measuring graphene adhesion using atomic force microscopy with a microsphere tip. Nanoscale 7 (24), 10760–10766.
Kitt, A.L., Qi, Z., Rémi, S., Park, H.S., Swan, A.K., Goldberg, B.B., 2013. How graphene slides: Measurement and theory of strain-dependent frictional forces between graphene and SiO2. Nano Lett. 13 (6), 2605–2610.
Komaragiri, U., Begley, M., Simmonds, J., 2005. The mechanical response of freestanding circular elastic films under point and pressure loads. J. Appl. Mech. 72 (2), 203–212.
Kumar, S., Parks, D.M., 2015. Strain shielding from mechanically activated covalent bond formation during nanoindentation of graphene delays the onset of failure. Nano Lett. 15 (3), 1503–1510.
Lee, G.-H., Cooper, R.C., An, S.J., Lee, S., Van Der Zande, A., Petrone, N., Hammerberg, A.G., Lee, C., Crawford, B., Oliver, W., et al., 2013. High-strength chemical-vapor–deposited graphene and grain boundaries. Science 340 (6136), 1073–1076.
Lee, J.H., Gao, Y., Bower, A.F., Xu, H., Pharr, G.M., 2018. Stiffness of frictional contact of dissimilar elastic solids. J. Mech. Phys. Solids 112, 318–333.
Lee, C., Wei, X., Kysar, J.W., Hone, J., 2008. Measurement of the elastic properties and intrinsic strength of monolayer graphene. Science 321 (5887), 385–388.
Lin, Q.-Y., Jing, G., Zhou, Y.-B., Wang, Y.-F., Meng, J., Bie, Y.-Q., Yu, D.-P., Liao, Z.-M., 2013. Stretch-induced stiffness enhancement of graphene grown by chemical vapor deposition. Acs Nano 7 (2), 1171–1177.
Lin, Q.-Y., Zeng, Y.-H., Liu, D., Jing, G.Y., Liao, Z.-M., Yu, D., 2014. Step-by-step fracture of two-layer stacked graphene membranes. ACS Nano 8 (10), 10246–10251.
Liu, K., Wu, J., 2016. Mechanical properties of two-dimensional materials and heterostructures. J. Mater. Res. 31 (7), 832–844.
Liu, K., Yan, Q., Chen, M., Fan, W., Sun, Y., Suh, J., Fu, D., Lee, S., Zhou, J., Tongay, S., et al., 2014. Elastic properties of chemical-vapor-deposited monolayer MoS2, WS2, and their bilayer heterostructures. Nano Lett. 14 (9), 5097–5103.
López-Polín, G., Gómez-Navarro, C., Parente, V., Guinea, F., Katsnelson, M.I., Perez-Murano, F., Gómez-Herrero, J., 2015. Increasing the elastic modulus of graphene by controlled defect creation. Nat. Phys. 11 (1), 26–31.
Majidi, C., Adams, G.G., 2009. A simplified formulation of adhesion problems with elastic plates. Proc. R. Soc. Lond. Ser. A Math. Phys. Eng. Sci. 465 (2107), 2217–2230.
Maner, K.C., Begley, M.R., Oliver, W.C., 2004. Nanomechanical testing of circular freestanding polymer films with sub-micron thickness. Acta Mater. 52 (19), 5451–5460.
Mansfield, E.H., 2005. The bending and stretching of plates. In: The Bending and Stretching of Plates. p. 240.
Manzanares-Negro, Y., López-Polín, G., Fujisawa, K., Zhang, T., Zhang, F., Kahn, E., Perea-López, N., Terrones, M., Gómez-Herrero, J., Gómez-Navarro, C., 2021. Confined crack propagation in MoS2 monolayers by creating atomic vacancies. ACS Nano 15 (1), 1210–1216.
Manzeli, S., Allain, A., Ghadimi, A., Kis, A., 2015. Piezoresistivity and strain-induced band gap tuning in atomically thin MoS2. Nano Lett. 15 (8), 5330–5335.
Mougin, J., Dupeux, M., Antoni, L., Galerie, A., 2003. Adhesion of thermal oxide scales grown on ferritic stainless steels measured using the inverted blister test. Mater. Sci. Eng. A 359 (1–2), 44–51.
Ozaki, T., Koga, T., Fujitsuka, N., Makino, H., Hohjo, H., Kadoura, H., 2018. Biaxial flexure testing of free-standing thin film membrane with nanoindentation system. Sensors Actuators A 278, 48–59.
Rao, Y., Kim, E., Dai, Z., He, J., Li, Y., Lu, N., 2023. Size-dependent shape characteristics of 2D crystal blisters. J. Mech. Phys. Solids 175, 105286.
Rao, Y., Qiao, S., Dai, Z., Lu, N., 2021. Elastic wetting: Substrate-supported droplets confined by soft elastic membranes. J. Mech. Phys. Solids 151, 104399.
Rokni, H., Lu, W., 2020. Direct measurements of interfacial adhesion in 2D materials and van der Waals heterostructures in ambient air. Nature Commun. 11 (1), 5607.
Ruiz-Vargas, C.S., Zhuang, H.L., Huang, P.Y., Van Der Zande, A.M., Garg, S., McEuen, P.L., Muller, D.A., Hennig, R.G., Park, J., 2011. Softened elastic response and unzipping in chemical vapor deposition graphene membranes. Nano Lett. 11 (6), 2259–2263.
Schwerin, E., 1929. Über spannungen und formänderungen kreisringförmiger membranen. Z. Angew. Math. Mech. 9 (6), 482–483.
Segovia, E.A.H., Torres-Torres, D., Higareda, J.R.P., García-García, A., 2021. Indentation size effects in graphene oxide under suspended nanoindentation. Mech. Mater. 158, 103875.
Shi, Q., Cheng, W., 2020. Free-standing 2D nanoassemblies. Adv. Funct. Mater. 30 (2), 1902301.
Suk, J.W., Mancevski, V., Hao, Y., Liechti, K.M., Ruoff, R.S., 2015. Fracture of polycrystalline graphene membranes by in situ nanoindentation in a scanning electron microscope. Phys. Status Solidi (RRL)–Rapid Res. Lett. 9 (10), 564–569.
Sun, Y., Wang, Y., Wang, E., Wang, B., Zhao, H., Zeng, Y., Zhang, Q., Wu, Y., Gu, L., Li, X., et al., 2022. Determining the interlayer shearing in twisted bilayer MoS2 by nanoindentation. Nature Commun. 13 (1), 3898.
Tu, Q., Spanopoulos, I., Yasaei, P., Stoumpos, C.C., Kanatzidis, M.G., Shekhawat, G.S., Dravid, V.P., 2018. Stretching and breaking of ultrathin 2D hybrid organic–inorganic perovskites. ACS Nano 12 (10), 10347–10354.
Vella, D., Davidovitch, B., 2017. Indentation metrology of clamped, ultra-thin elastic sheets. Soft Matter 13 (11), 2264–2278.
Wan, K.-T., Guo, S., Dillard, D.A., 2003. A theoretical and numerical study of a thin clamped circular film under an external load in the presence of a tensile residual stress. Thin Solid Films 425 (1–2), 150–162.
Wang, Z., Sheng, H., Lin, X., Rao, Y., Liu, J., Lu, N., 2024b. A shear-lag model for laminated beams with extreme modulus mismatch between layers. Mech. Mater. 188, 104844.
Wang, X., Tian, H., Xie, W., Shu, Y., Mi, W.-T., Ali Mohammad, M., Xie, Q.-Y., Yang, Y., Xu, J.-B., Ren, T.-L., 2015. Observation of a giant two-dimensional band-piezoelectric effect on biaxial-strained graphene. NPG Asia Mater. 7 (1), e154–e154.

Wang, R., Ying, T., Chen, Y., Zhu, F., Leng, J., Chang, T., Zhang, T., Gao, H., 2024a. A generalizable framework of solution-guided machine learning with application to nanoindentation of free-standing thin films. Thin-Walled Struct. 111984.
Yang, Y., Yang, X., Liang, L., Gao, Y., Cheng, H., Li, X., Zou, M., Ma, R., Yuan, Q., Duan, X., 2019. Large-area graphene-nanomesh/carbon-nanotube hybrid membranes for ionic and molecular nanofiltration. Science 364 (6445), 1057–1062.
Yuan, W., Wang, G., 2021. Adhesion between a rigid sphere and a stretched membrane using the dugdale model. Int. J. Solids Struct. 208, 214–220.
Zhan, H., Tan, X., Xie, G., Guo, D., 2021. Load-dependent energy dissipation induced by the tip–membrane friction on suspended 2D materials. Phys. Chem. Chem. Phys. 23 (35), 19819–19826.
Zhang, X., Yu, K., Lang, H., Huang, Y., Peng, Y., 2023. Friction reduction of suspended multilayer h-BN based on electrostrain. Appl. Surf. Sci. 611, 155312.
Zhang, J., Zhou, Y., Ying, P., Sun, H., Zhou, J., Wang, T., Jie, W., Kuball, M., 2020. Effects of interlayer interactions on the nanoindentation response of freely suspended multilayer gallium telluride. Nanotechnology 31 (16), 165706.
Zhou, L., Wang, Y., Cao, G., 2013a. Boundary condition and pre-strain effects on the free standing indentation response of graphene monolayer. J. Phys.: Condens. Matter. 25 (47), 475303.
Zhou, L., Wang, Y., Cao, G., 2013b. van der Waals effect on the nanoindentation response of free standing monolayer graphene. Carbon 57, 357–362.
Zhou, L., Xue, J., Wang, Y., Cao, G., 2013c. Molecular mechanics simulations of the deformation mechanism of graphene monolayer under free standing indentation. Carbon 63, 117–124.
Zhupanska, O., 2009. Axisymmetric contact with friction of a rigid sphere with an elastic half-space. Proc. R. Soc. Lond. Ser. A Math. Phys. Eng. Sci. 465 (2108), 2565–2588.